

# The properties and polarization of the H<sub>2</sub>O and CH<sub>3</sub>OH maser environment of NGC7538-IRS 1

G. Surcis <sup>\*,1</sup>, W.H.T. Vlemmings<sup>1</sup>, R.M. Torres<sup>1</sup>, H.J. van Langevelde<sup>2,3</sup>, and B. Hutawarakorn Kramer<sup>4,5</sup>

<sup>1</sup> Argelander-Institut für Astronomie der Universität Bonn, Auf dem Hügel 71, 53121 Bonn, Germany  
e-mail: gsurcis@astro.uni-bonn.de

<sup>2</sup> Joint Institute for VLBI in Europe, Postbus 2, 79990 AA Dwingeloo, The Netherlands

<sup>3</sup> Sterrewacht Leiden, Leiden University, Postbus 9513, 2300 RA Leiden, The Netherlands

<sup>4</sup> Max-Planck Institut für Radioastronomie, Auf dem Hügel 69, 53121 Bonn, Germany

<sup>5</sup> National Astronomical Research Institute of Thailand, Ministry of Science and Technology, Rama VI Rd., Bangkok 10400, Thailand

Received ; accepted

## ABSTRACT

**Context.** NGC7538 is a complex massive star-forming region. The region is composed of several radio continuum sources, one of which is IRS 1, a high-mass protostar, from which a 0.3 pc molecular bipolar outflow was detected. Several maser species have been detected around IRS 1. The CH<sub>3</sub>OH masers have been suggested to trace a Keplerian-disk, while the H<sub>2</sub>O masers are almost aligned to the outflow. More recent results suggested that the region hosts a torus and potentially a disk, but with a different inclination than the Keplerian-disk that is supposed to be traced by the CH<sub>3</sub>OH masers.

**Aims.** Tracing the magnetic field close to protostars is fundamental for determining the orientation of the disk/torus. Recent studies showed that during the protostellar phase of high-mass star formation the magnetic field is oriented along the outflows and around or on the surfaces of the disk/torus. The observations of polarized maser emissions at milliarcsecond resolution can make a crucial contribution to understanding the orientation of the magnetic field and, consequently, the orientation of the disk/torus in NGC7538-IRS 1.

**Methods.** The NRAO Very Long Baseline Array was used to measure the linear polarization and the Zeeman-splitting of the 22 GHz H<sub>2</sub>O masers toward NGC7538-IRS 1. The European VLBI Network and the MERLIN telescopes were used to measure the linear polarization and the Zeeman-splitting of the 6.7 GHz CH<sub>3</sub>OH masers toward the same region.

**Results.** We detected 17 H<sub>2</sub>O masers and 49 CH<sub>3</sub>OH masers at high angular resolution. We detected linear polarization emission toward two H<sub>2</sub>O masers and toward twenty CH<sub>3</sub>OH masers. The CH<sub>3</sub>OH masers, most of which only show a core structure, seem to trace rotating and potentially infalling gas in the inner part of a torus. Significant Zeeman-splitting was measured in three CH<sub>3</sub>OH masers. No significant (3 $\sigma$ ) magnetic field strength was measured using the H<sub>2</sub>O masers. We also propose a new description of the structure of the NGC7538-IRS 1 maser region.

**Key words.** Stars: formation - masers: water, methanol - polarization - magnetic fields - ISM: individual: NGC7538

## 1. Introduction

NGC7538 is a complex massive star-forming region located in the Perseus arm of our Galaxy at a distance of 2.65 kpc (Moscadelli et al. 2009). The region is composed of several clusters of infrared sources (Wynn-Williams et al. 1974) and radio continuum sources (Campbell 1984). The brightest source is NGC7538-IRS 1, whose central star has been suggested to be an O6 star of about 30 M<sub>⊙</sub> with systemic local standard of rest velocity  $V_{\text{lsr}} = -58 \text{ km s}^{-1}$  (Campbell & Thompson 1984; Sandell et al. 2009; Puga et al. 2010). Several high-velocity molecular bipolar outflows were detected in NGC7538 and one of these is elongated 0.3 pc from IRS 1 (position angle PA=140°) with a velocity of 250 km s<sup>-1</sup> and a mass of 82.8 M<sub>⊙</sub> (Kameya et al. 1989; Gaume et al. 1995; Davis et al. 1998; Qiu et al. 2011). VLA continuum observations by Campbell (1984) indicate that the PA of the outflow decreases away from IRS 1; i.e., 180° at 0''.3 (0.004 pc) and 165° at 2'' (0.03 pc). Kameya et al. (1989) gave three possible interpretations of this rotation: disk precession, interaction of the flow with dense gas, and cou-

pling of the gas with a large-scale magnetic field around IRS 1. Because Sandell et al. (2009) found that the collimated free-free jet (opening angle  $\lesssim 30^\circ$ ) is approximately aligned with the outflow and that there is a strong accretion flow toward IRS 1 (accretion rate  $\sim 2 \times 10^{-4} \text{ M}_\odot \text{ yr}^{-1}$ ), IRS 1 must be surrounded by an accretion disk. The morphology of the free-free emission, which is optically thick up to 100 GHz (Franco-Hernández & Rodríguez 2004), suggests that the disk should be almost edge-on and oriented east-west (Scoville et al. 2008; Kameya et al. 1989; Sandell et al. 2009). A possible detection of this edge-on disk was made by Minier et al. (1998), who observed a linear distribution of the brightest CH<sub>3</sub>OH masers with an inclination angle of about 112°. Pestalozzi et al. (2004) estimated that this disk is a Keplerian disk with an outer radius of  $\sim 750 \text{ AU}$  and an inner radius of  $\sim 290 \text{ AU}$  by modeling the CH<sub>3</sub>OH maser emissions at 6.7 and 12.2-GHz.

Recent results disagree with the edge-on disk traced by the CH<sub>3</sub>OH masers. The observations of the mid-infrared emission suggest that the radio continuum emission does not come from a free-free jet but that it traces the ionized gas wind from the disk surface that in the new scenario would be perpendicular to the CO-bipolar outflow with a disk inclination angle  $i = 32^\circ$  (De Buizer & Minier 2005). Klaassen et al. (2009) ob-

\* Member of the International Max Planck Research School (IMPRS) for Astronomy and Astrophysics at the Universities of Bonn and Cologne.

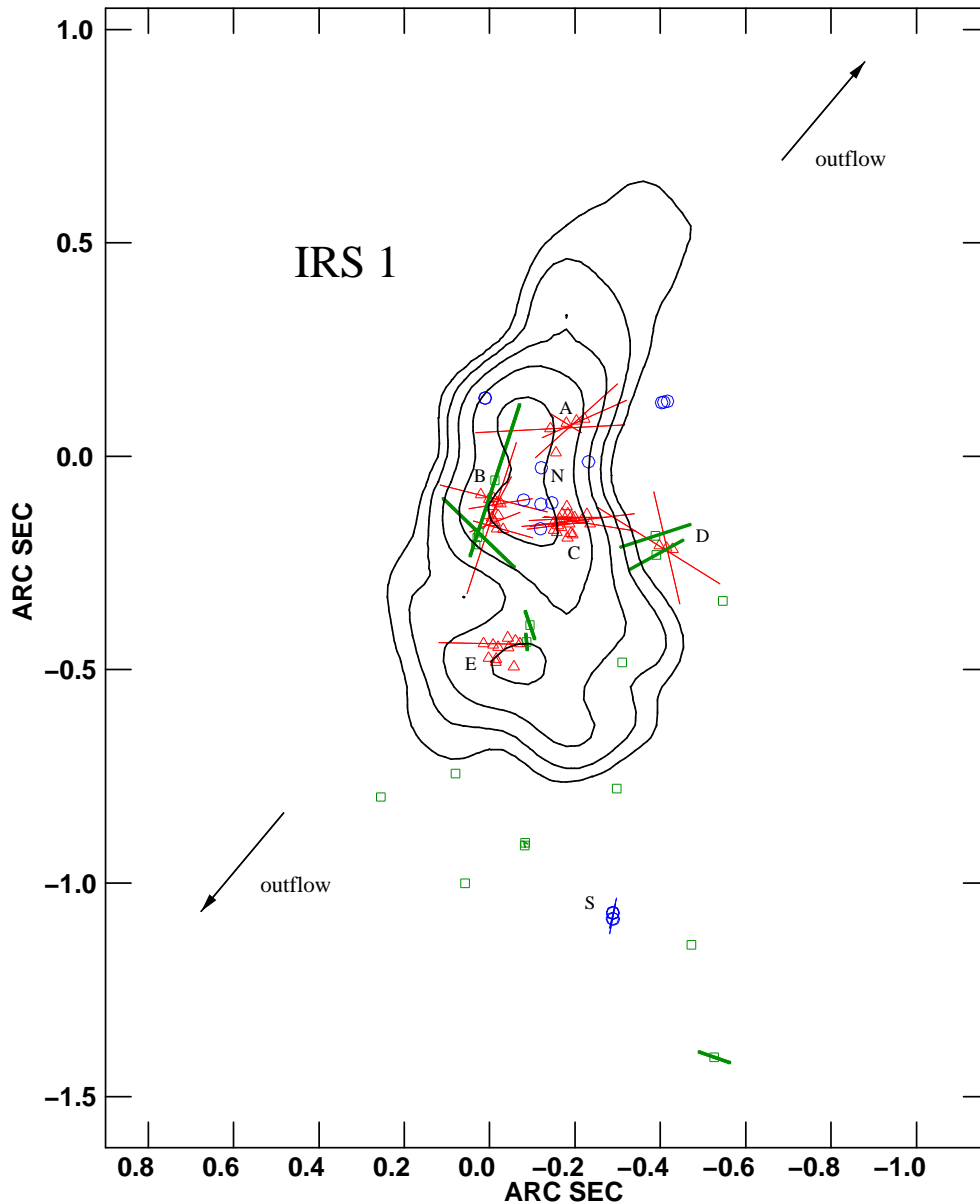


**Fig. 1.** Positions of water, methanol, and hydroxyl maser features superimposed on the 2 cm continuum contour map of NGC7538-IRS 1 observed with the VLA in 1986 (Franco-Hernández & Rodríguez 2004). Contours are 1, 2, 4, 8, 16  $\times 1.3$  mJy beam $^{-1}$ . The (0,0) position is  $\alpha_{2000} = 23^{\text{h}}13^{\text{m}}45^{\text{s}}.382$  and  $\delta_{2000} = +61^{\circ}28'10''.441$ . Blue circles and red triangles indicate the positions of the H<sub>2</sub>O and CH<sub>3</sub>OH maser features, respectively, with their linear polarization vectors (60 mas correspond to a linear polarization fraction of 1%). Green boxes indicate the positions of the OH masers detected by Hutawarakorn & Cohen (2003) with their linear polarization vectors (thick lines, 6 mas correspond to 1%). The two arrows indicate the direction of the bipolar outflow ( $\sim 140^{\circ}$ ).

served two warm gas tracers (SO<sub>2</sub> and OCS) toward NGC7538-IRS 1 with the Submillimeter Array (SMA). Although the region was unresolved, they found a velocity gradient consistent with the CH<sub>3</sub>OH maser velocities and perpendicular to the large-scale molecular bipolar outflow. This rotating gas might indicate that there is a torus (with an angular size of about 2 arcsec; i.e.,  $\sim 5300$  AU at 2.65 kpc) surrounding the smaller accretion disk proposed by De Buizer & Minier (2005).

In addition, Krauss et al. (2006) proposed two possible scenarios for NGC7538-IRS 1 by considering both the linear distribution of the 6.7-GHz CH<sub>3</sub>OH masers detected previously (e.g., Pestalozzi et al. 2004, De Buizer & Minier 2005) and the asymmetry in the near infrared (NIR) images observed by them. In their most likely scenario, called “Scenario B”,

the CH<sub>3</sub>OH masers trace the edge-on disk as suggested by Pestalozzi et al. (2004) and the asymmetry might be caused by the precession of the jet. In the “Scenario A” the CH<sub>3</sub>OH masers do not trace a disk but an outflow cavity as proposed by De Buizer & Minier (2005), where the detected asymmetry might simply reflect the innermost walls of this cavity.

Besides the CH<sub>3</sub>OH masers, other maser species were detected around NGC7538-IRS 1: OH, H<sub>2</sub>O, NH<sub>3</sub>, and H<sub>2</sub>CO (e.g., Hutawarakorn & Cohen 2003; Galván-Madrid et al. 2010; Gaume et al. 1991; Hoffman et al. 2003). The OH masers are located southward and show no obvious disk structure or relation to the outflow direction (Hutawarakorn & Cohen 2003). H<sub>2</sub>CO and H<sub>2</sub>O masers are located near the center of the continuum emission, and the H<sub>2</sub>O masers are also almost aligned with

**Table 1.** All 22 GHz H<sub>2</sub>O maser features detected in NGC7538-IRS 1.

(1) Maser	(2) Group	(3) RA offset (mas)	(4) Dec offset (mas)	(5) Peak flux Density(I) (Jy beam <sup>-1</sup> )	(6) V <sub>lsr</sub> (km s <sup>-1</sup> )	(7) Δv <sub>L</sub> (km s <sup>-1</sup> )	(8) P <sub>l</sub> (%)	(9) χ <sup>a</sup> (°)	(10) ΔV <sub>i</sub> <sup>a</sup> (km s <sup>-1</sup> )	(11) T <sub>b</sub> ΔΩ <sup>a</sup> (log K sr)	(12) P <sub>V</sub> <sup>b</sup> (%)	(13) θ <sup>c</sup> (°)
W01	N	-185.2131	141.908	17.11 ± 0.07	-57.8	0.41	—	—	—	—	—	—
W02	N	-176.4676	139.422	1.00 ± 0.02	-58.3	0.32	—	—	—	—	—	—
W03	N	-170.9744	139.088	0.48 ± 0.02	-58.3	0.27	—	—	—	—	—	—
W04	S	-57.6929	-1071.104	0.90 ± 0.01	-72.2	0.59	—	—	—	—	—	—
W05	S	-57.4470	-1056.554	0.48 ± 0.01	-57.3	0.47	—	—	—	—	—	—
W06	S	-57.3376	-1056.630	36.43 ± 0.02	-70.3	1.15	1.2 ± 0.1	-13.0 ± 1.3	—	—	—	—
W07	S	-57.1463	-1057.065	16.99 ± 0.01	-73.3	0.77	1.2 ± 0.1	-10.8 ± 0.5	3.4 <sup>+0.1</sup> <sub>-0.3</sub>	9.1 <sup>+0.3</sup> <sub>-0.1</sub>	0.37 ± 0.13	81 <sup>+9</sup> <sub>-13</sub>
W08	S	-56.7637	-1056.586	0.15 ± 0.01	-67.3	1.46	—	—	—	—	—	—
W09	S	-56.4631	-1070.080	0.48 ± 0.01	-71.6	0.64	—	—	—	—	—	—
W10	N	0	0	7.34 ± 0.03	-60.6	0.56	—	—	—	—	—	—
W11	N	85.5692	-96.002	0.36 ± 0.02	-59.7	0.44	—	—	—	—	—	—
W12	N	110.0019	-13.538	0.20 ± 0.03	-60.2	0.83	—	—	—	—	—	—
W13	N	111.6690	-99.499	9.31 ± 0.03	-60.1	0.47	—	—	—	—	—	—
W14	N	112.8442	-156.492	0.25 ± 0.03	-60.1	0.42	—	—	—	—	—	—
W15	N	151.9803	-90.046	1.04 ± 0.03	-59.9	0.40	—	—	—	—	—	—
W16	N	242.0042	148.947	0.13 ± 0.01	-43.3	0.62	—	—	—	—	—	—
W17	N	242.7694	149.715	0.14 ± 0.01	-43.8	0.59	—	—	—	—	—	—

**Notes.** <sup>(a)</sup> The best-fitting results obtained by using a model based on the radiative transfer theory of H<sub>2</sub>O masers for  $\Gamma + \Gamma_v = 1\text{ s}^{-1}$  (Surcis et al. 2011). The errors were determined by analyzing the full probability distribution function. <sup>(b)</sup> The percentage of circular polarization is given by  $P_V = (V_{\max} - V_{\min})/I_{\max}$ . <sup>(c)</sup> The angle between the magnetic field and the maser propagation direction is determined by using the observed  $P_l$  and the fitted emerging brightness temperature. The errors were determined by analyzing the full probability distribution function.

the outflow (Galván-Madrid et al. 2010). The 6.7 and 12.2-GHz CH<sub>3</sub>OH masers show a cone shape that opens to the north-west (Minier et al. 2000).

So far, the magnetic field structure in NGC7538-IRS 1 has been studied using submillimeter imaging polarimetry (Momose et al. 2001) and OH maser emission (Hutawarakorn & Cohen 2003). Although the polarization vectors are locally disturbed, at an angular resolution of 14 arcsec the magnetic field directions agree with the direction of the outflow (Momose et al. 2001), while at milliarcsecond (mas) resolution the OH maser observations indicate a magnetic field oriented orthogonal to the outflow (Hutawarakorn & Cohen 2003). Because H<sub>2</sub>O and CH<sub>3</sub>OH masers were detected close to the center of the continuum emission, i.e. to the protostar, it is worthwhile investigating their linear and circular polarization emissions. As shown by Surcis et al. (2009, 2011) for the massive star-forming region W75N, the polarization observations of the two maser species can depict a reasonable scenario for the magnetic field close to massive protostars. Moreover, the direction and strength of the magnetic field might help to decide the debate about the orientation of the disk.

Here we present Very Long Baseline Array (VLBA) observations of H<sub>2</sub>O masers, Multi-Element Radio Linked Interferometer network (MERLIN) and European VLBI Network (EVN) observations of CH<sub>3</sub>OH masers in full polarization toward NGC7538-IRS 1. In Sect. 3 we show our results obtained by studying the linear and circular polarization of H<sub>2</sub>O and CH<sub>3</sub>OH maser emissions in a similar way as Vlemmings et al. (2006, 2010) and Surcis et al. (2009, 2011) for Cepheus A and W75N, respectively. In Sect. 4 we discuss our results and attempt to disentangle the complex morphology in NGC7538-IRS 1.

## 2. Observations and analysis

### 2.1. 22 GHz VLBA data

We observed the star-forming region NGC7538-IRS1 in the 6<sub>16</sub>-5<sub>23</sub> transition of H<sub>2</sub>O (rest frequency: 22.23508 GHz) with the

NRAO<sup>1</sup> VLBA on November 21, 2005. The observations were made in full polarization spectral mode using four overlapped baseband filters of 1 MHz to cover a total velocity range of  $\approx 50$  km s<sup>-1</sup>. Two correlations were performed. One with 128 channels to generate all four polarization combinations (RR, LL, RL, LR) with a channel width of 7.8 kHz (0.1 km s<sup>-1</sup>). The other one with high spectral resolution (512 channels; 1.96 kHz=0.027 km s<sup>-1</sup>), which only contains the circular polarization combinations (LL, RR), to be able to detect Zeeman-splitting of the H<sub>2</sub>O maser across the entire velocity range. Including the overheads, the total observation time was 8 h.

The data were edited and calibrated using the Astronomical Image Processing System (AIPS) following the method of Kembell et al. (1995). The bandpass, the delay, the phase, and the polarization calibration were performed on the calibrator J0359+5057. The fringe-fitting and the self-calibration were performed on the brightest maser feature (W06 in Table 1). All calibration steps were initially performed on the dataset with modest spectral resolution after which the solutions, with the exception of the bandpass solutions that were obtained separately, were copied and applied to the high spectral resolution dataset. Stokes  $I$ ,  $Q$ , and  $U$  data cubes (4 arcsec  $\times$  4 arcsec, rms  $\approx 7$  mJy beam<sup>-1</sup>) were created using the AIPS task IMAGR (beam-size 1.0 mas  $\times$  0.4 mas) from the modest spectral resolution dataset, while the  $I$  and  $V$  cubes (rms  $\approx 8$  mJy beam<sup>-1</sup>) were imaged from the high spectral resolution dataset and for the same fields. The  $Q$  and  $U$  cubes were combined to produce cubes of polarized intensity and polarization angle. Because these observations were obtained between two VLA polarization calibration observations<sup>2</sup> made by the NRAO in 2009, during which the linear polarization angle of J0359+5057 was constant at  $-86^\circ 7'$ , we were able to estimate the polarization angles with a systemic error of no more than  $\sim 3^\circ$ .

We identified the H<sub>2</sub>O maser features using the process described in Surcis et al. (2011). Here the program called “maser finder” is used. This program is able to search maser spots, ve-

<sup>1</sup> The National Radio Astronomy Observatory (NRAO) is a facility of the National Science Foundation operated under cooperative agreement by Associated Universities, Inc.

<sup>2</sup> <http://www.aoc.nrao.edu/smyers/calibration/>

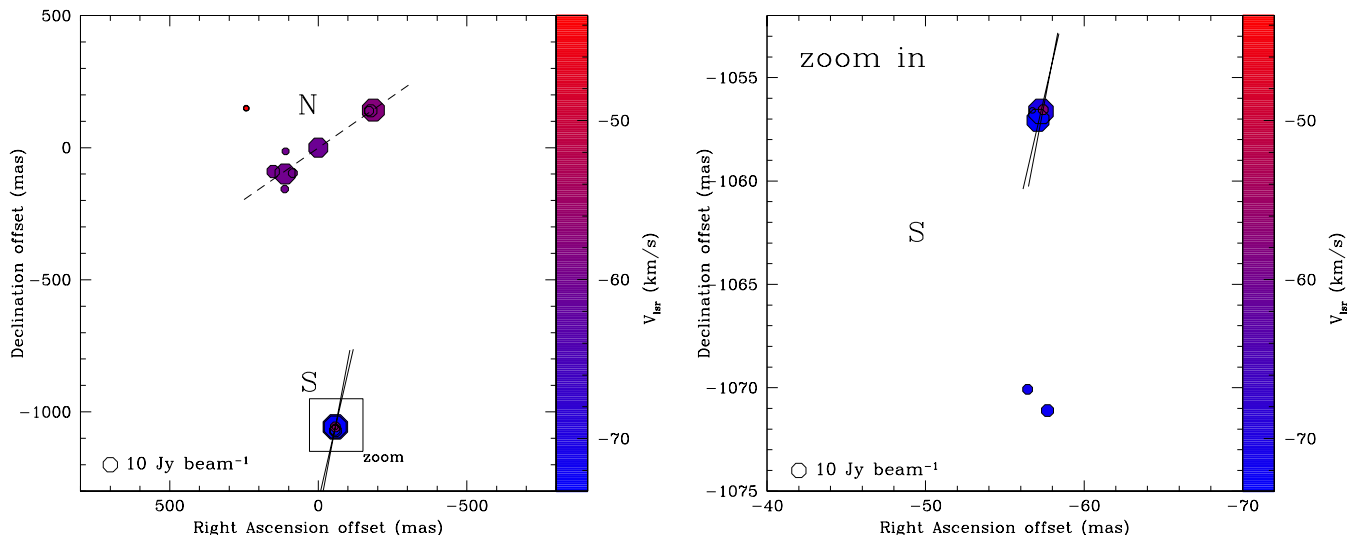


**Fig. 2.** Left panel: a close-up view of the H<sub>2</sub>O maser features around NGC7538-IRS1. Right panel: a zoom-in view of the boxed region of the left panel. The octagonal symbols are the identified maser features in the present work scaled logarithmically according to their peak flux density. The maser LSR radial velocity is indicated by color. A 10 Jy beam<sup>-1</sup> symbol is plotted for illustration in both panels. The reference position is  $\alpha_{2000} = 23^{\text{h}}13^{\text{m}}45^{\text{s}}.350$  and  $\delta_{2000} = +61^{\circ}28'10''.428$ , which was estimated as described in Sect. 3. The linear polarization vectors, scaled logarithmically according to polarization fraction  $P_1$  (in Table 1), are overplotted. The dashed line (PA=-52°) is the result of the best linear fit of the H<sub>2</sub>O masers of group N (features W16 and W17 were not included). The synthesized beam is 1.0 mas  $\times$  0.4 mas.

locity channel by velocity channel. We identified a maser feature when three or more maser spots coincide spatially (within a box 2 by 2 pixels) and each of them appeared in consecutive velocity channels. In Table 1 only the brightest spot of each series of maser spots that fulfill the criteria described above are reported. The two maser features that show linear polarization emission were fitted using a full radiative transfer method code based on the models for H<sub>2</sub>O masers of Nedoluha & Watson (1992). They solved the transfer equations for the polarized radiation of 22 GHz H<sub>2</sub>O masers in the presence of a magnetic field which causes a Zeeman-splitting that is much smaller than spectral line breadth. The fit provides the emerging brightness temperature ( $T_b\Delta\Omega$ ) and the intrinsic thermal linewidth ( $\Delta V_i$ ). See Vlemmings et al. (2006) and Surcis et al. (2011) for more details. We modeled the observed linear polarized and total intensity maser spectra by gridding  $\Delta V_i$  from 0.5 to 3.5 km s<sup>-1</sup>, in steps of 0.025 km s<sup>-1</sup>, by using a least-squares fitting routine. From the fit results we were able to determine the best values of the angle between the maser propagation direction and the magnetic field ( $\theta$ ). By considering the values of  $T_b\Delta\Omega$ ,  $\Delta V_i$ , and  $\theta$  we were also able to estimate the saturation state of the H<sub>2</sub>O maser features.

## 2.2. 6.7 GHz MERLIN data

To detect the polarization of the CH<sub>3</sub>OH maser emission at 6668.518 MHz ( $5_1 - 6_0$  A<sup>+</sup>) we observed NGC7538-IRS1 with six of the MERLIN<sup>3</sup> telescopes in full polarization spectral mode on December 28, 2005. The observation time was  $\sim 2$  h, including overheads on the calibrators 2300+638, 3C84 and 3C286. We used a 250 kHz bandwidth ( $\sim 11$  km s<sup>-1</sup>) with 256 channels (velocity resolution  $\sim 0.04$  km s<sup>-1</sup>) centered on the source ve-

locity  $V_{\text{lsr}} = -56.1$  km s<sup>-1</sup>. For calibration purposes, the continuum calibrators were observed with the 16 MHz wide-band mode. Both 3C84 and 3C286 were also observed in the narrow-band spectral line configuration and were used to determine the flux and bandpass calibration solutions. The data were edited and calibrated using AIPS. The calibrator 3C84 was used to determine the phase offset between the wide- and narrow-band set-up. Instrumental feed polarization was determined using the unpolarized calibrator 3C84, and the polarization angle was calibrated using 3C286. Using one of the strongest isolated maser features, we were able to self-calibrate the data in right- and left-circular polarization separately. After calibration, the antenna contributions were reweighed according to their sensitivity at 5 GHz and their individual efficiency. Stokes  $I$ ,  $Q$ ,  $U$  data cubes (5.12 arcsec  $\times$  5.12 arcsec, rms  $\approx 10$  mJy beam<sup>-1</sup>) were created (beam-size 47 mas  $\times$  34 mas).

The CH<sub>3</sub>OH maser features were also identified through the identification process mentioned above (Surcis et al. 2011). If the program finds a group of maser spots that are not exactly spatially coincident but show a continuum linear distribution with a clear velocity gradient, we report in the corresponding table only the brightest maser spot of the group (e.g. maser feature M06). We were unable to identify weak CH<sub>3</sub>OH maser features ( $< 1$  Jy beam<sup>-1</sup>) close to the brightest ones because of the dynamic range limits. To determine  $T_b\Delta\Omega$ ,  $\Delta V_i$ , and  $\theta$ , we adapted the code used for 22 GHz H<sub>2</sub>O masers to model the 6.7 GHz CH<sub>3</sub>OH masers, which has successfully been used by Vlemmings et al. (2010) for the CH<sub>3</sub>OH masers in Cepheus A. We modeled the observed linear polarized and total intensity CH<sub>3</sub>OH maser feature spectra by gridding  $\Delta V_i$  from 0.5 to 2.6 km s<sup>-1</sup>, in steps of 0.05 km s<sup>-1</sup>, by using a least-squares fitting routine.

<sup>3</sup> MERLIN is operated by the University of Manchester as a National Facility of the Science and Technology Facilities Council

**Table 2.** All 6.7 GHz CH<sub>3</sub>OH maser features detected in NGC7538-IRS 1 with MERLIN.

(1) Maser	(2) group	(3) RA <sup>a</sup> offset (mas)	(4) Dec <sup>a</sup> offset (mas)	(5) Peak flux Density(I) (Jy beam <sup>-1</sup> )	(6) V <sub>lsr</sub> (km s <sup>-1</sup> )	(7) Δv <sub>L</sub> (km s <sup>-1</sup> )	(8) P <sub>l</sub> (%)	(9) χ <sup>c</sup> (°)	(10) ΔV <sub>i</sub> <sup>b</sup> (km s <sup>-1</sup> )	(11) T <sub>b</sub> ΔΩ <sup>b</sup> (log K sr)	(12) θ <sup>c</sup> (°)
M01	D	-256	-275	22.91 ± 0.01	-60.68	0.86	7.1 ± 1.4	+39 ± 8	< 0.55 <sup>d</sup>	> 12 <sup>d</sup>	—
M02	A	-115	47	1.70 ± 0.02	-55.94	0.45	—	—	—	—	—
M03	A	-74	22	23.53 ± 0.01	-57.30	0.36	1.3 ± 0.6	-47 ± 3	1.20 <sup>+0.08</sup> <sub>-0.15</sub>	8.7 <sup>+0.1</sup> <sub>-1.3</sub>	90 <sup>+53</sup> <sub>-53</sub>
M04	C	-73	-215	51.32 ± 0.01	-61.38	0.37	1.3 ± 0.4	-42 ± 4	—	—	—
M05	C	-28	-222	50.53 ± 0.01	-60.81	0.85	0.7 ± 0.4	+41 ± 8	2.20 <sup>+0.06</sup> <sub>-0.13</sub>	8.4 <sup>+0.3</sup> <sub>-1.0</sub>	76 <sup>+11</sup> <sub>-46</sub>
M06	A	0	0	172.00 ± 0.02	-56.07	0.63	1.0 ± 0.4	+45 ± 60	< 0.95 <sup>d</sup>	> 12 <sup>d</sup>	—
M07	B	59	-287	3.88 ± 0.01	-58.44	0.52	1.5 ± 0.9	-29 ± 7	—	—	—
M08	B	98	-186	1.11 ± 0.01	-58.70	0.54	—	—	—	—	—
M09	E	87	-559	3.54 ± 0.01	-59.05	0.31	1.6 ± 0.2	+33 ± 6	1.40 <sup>+0.08</sup> <sub>-0.12</sub>	8.8 <sup>+0.4</sup> <sub>-0.3</sub>	87 <sup>+4</sup> <sub>-20</sub>
M10	E	125	-546	1.08 ± 0.01	-58.83	0.42	—	—	—	—	—
M11	B	127	-207	24.41 ± 0.01	-57.61	0.70	0.5 ± 0.1	-23 ± 15	< 0.90 <sup>d</sup>	> 12 <sup>d</sup>	—
M12	E	154	-503	61.83 ± 0.01	-58.09	0.30	0.4 ± 0.1	+10 ± 5	1.65 <sup>+0.05</sup> <sub>-0.08</sub>	8.2 <sup>+0.7</sup> <sub>-0.3</sub>	72 <sup>+10</sup> <sub>-44</sub>
M13	B	159	-157	9.71 ± 0.02	-56.33	0.40	1.6 ± 1.3	+18 ± 13	—	—	—

**Notes.** <sup>(a)</sup> The absolute reference position is  $\alpha_{2000} = 23^{\text{h}}13^{\text{m}}45^{\text{s}}.362$  and  $\delta_{2000} = +61^{\circ}28'10''.506$ . <sup>(b)</sup> The best-fitting results obtained by using a model based on the radiative transfer theory of CH<sub>3</sub>OH masers for  $\Gamma + \Gamma_{\nu} = 1\text{s}^{-1}$  (Vlemmings et al. 2010). The errors were determined by analyzing the full probability distribution function. <sup>(c)</sup> The angle between the magnetic field and the maser propagation direction is determined by using the observed  $P_l$  and the fitted emerging brightness temperature. The errors were determined by analyzing the full probability distribution function. <sup>(d)</sup> Because of the low angular resolution the code is able to give an upper limit for  $\Delta V_i$  and a lower limit for  $T_b\Delta\Omega$ .

### 2.3. 6.7 GHz EVN data

NGC7538-IRS1 was also observed at 6.7 GHz (CH<sub>3</sub>OH) in full polarization spectral mode with nine of the EVN<sup>4</sup> antennas (Jodrell2, Cambridge, Efelsberg, Onsala, Medicina, Torun, Noto, Westerbork, and the new joint antenna Yebes-40m), for a total observation time of 5 h on November 3, 2009 (program code ES063B). The bandwidth was 2 MHz, providing a velocity range of  $\sim 100\text{ km s}^{-1}$ . The data were correlated using 1024 channels to generate all four polarization combinations (RR, LL, RL, LR) with a spectral resolution of 1.9 kHz ( $\sim 0.1\text{ km s}^{-1}$ ).

The data were edited and calibrated using AIPS. The band-pass, the delay, the phase, and the polarization calibration were performed on the calibrator 3C286. Fringe-fitting and self-calibration were performed on the brightest maser feature (E26 in Table 3). Then we imaged the  $I$ ,  $Q$ ,  $U$ ,  $RR$ , and  $LL$  cubes ( $2\text{ arcsec} \times 2\text{ arcsec}$ ,  $\text{rms} \approx 8\text{ mJy beam}^{-1}$ ) using the AIPS task IMAGR (beam-size  $6.3\text{ mas} \times 4.9\text{ mas}$ ). The  $Q$  and  $U$  cubes were combined to produce cubes of polarized intensity and polarization angle.

In this case, because the dynamic range of our EVN observations was better than that of MERLIN observations, we were able to identify CH<sub>3</sub>OH maser features with a peak flux density of less than  $1\text{ Jy beam}^{-1}$  with the “maser finder” program. The maser emission was fitted by using the adapted code for CH<sub>3</sub>OH masers, but with a grid of  $\Delta V_i$  ranging from 0.5 to  $1.95\text{ km s}^{-1}$ . We were able to determine the Zeeman-splitting from the cross-correlation between the RR and LL spectra, which was successfully used by Surcis et al. (2009) for the polarized CH<sub>3</sub>OH maser emission detected in W75N. The dynamic range of the RR and LL cubes decreases close to the strongest maser emission of each group because of the residual calibration errors. As a result, we were not able to determine the Zeeman-splitting ( $\Delta V_Z$ ) for the features with a peak flux density of less than  $1.8\text{ Jy beam}^{-1}$ .

## 3. Results

In Fig. 1 we show the H<sub>2</sub>O (blue circles) and CH<sub>3</sub>OH maser features (red triangles) detected by us and superimposed on

<sup>4</sup> The European VLBI Network is a joint facility of European, Chinese, South African and other radio astronomy institutes funded by their national research councils.

the 2 cm continuum contour map of NGC7538-IRS1 observed with the VLA in 1986 (Franco-Hernández & Rodríguez 2004). Because the continuum observations were made 20.3 yr before our observations, we have shifted the continuum map by  $-50\text{ mas}$  in both directions according to the proper motion,  $\mu_{\alpha} = -2.45\text{ mas yr}^{-1}$  and  $\mu_{\delta} = -2.45\text{ mas yr}^{-1}$ , measured by Moscadelli et al. (2009). The direction of the large-scale molecular bipolar outflow is also shown. Because we did not have absolute positions of the H<sub>2</sub>O maser features, we estimated the offset of one common H<sub>2</sub>O maser feature detected both in the VLA observations of Galván-Madrid et al. (2010) and by us (features M3 and W01, respectively). All positions of the H<sub>2</sub>O maser features were shifted according to this offset. We did indeed have absolute positions of the CH<sub>3</sub>OH maser features at low-angular resolution, but not at high-angular resolution. Hence, to overlay these maser features to the continuum, we matched the brightest CH<sub>3</sub>OH maser feature detected with the EVN and the brightest one detected with MERLIN (M06, absolute position  $\alpha_{2000} = 23^{\text{h}}13^{\text{m}}45^{\text{s}}.362$  and  $\delta_{2000} = +61^{\circ}28'10''.506$ ). All CH<sub>3</sub>OH maser features were shifted accordingly. Thus, based on the resolution of the VLA H<sub>2</sub>O and MERLIN CH<sub>3</sub>OH maser observations the uncertainties of H<sub>2</sub>O and CH<sub>3</sub>OH maser features absolute positions are 50 mas (Galván-Madrid et al. 2010) and 10 mas, respectively.

### 3.1. H<sub>2</sub>O masers

We detected 17 22-GHz H<sub>2</sub>O maser features with the VLBA associated to NGC7538-IRS1 (named W01-W17 in Table 1). No H<sub>2</sub>O maser emission with a peak flux density ( $I$ ) less than  $0.13\text{ Jy beam}^{-1}$  is detected even though our channel rms is significantly less.

The H<sub>2</sub>O maser features can be divided into two groups, N and S, that are composed of 11 and 6 H<sub>2</sub>O maser features, respectively. Group N is located at the center of the continuum emission and it shows a linear distribution with a position angle of  $-52^{\circ}$  (see Fig. 2). The local standard-of-rest velocities ( $V_{\text{lsr}}$ ) of group N are between  $-60.2\text{ km s}^{-1}$  and  $-43.3\text{ km s}^{-1}$ . Excluding W16 and W17, the range is  $-60.2\text{ km s}^{-1} < V_{\text{lsr}}^{\text{N}} < -58.3\text{ km s}^{-1}$ . Group S is located about  $1''$  southward from group N and its velocity range is  $-73.3\text{ km s}^{-1} < V_{\text{lsr}}^{\text{S}} < -57.3\text{ km s}^{-1}$ , which is more blue-shifted.

Linear polarization is detected in 2 H<sub>2</sub>O maser features that

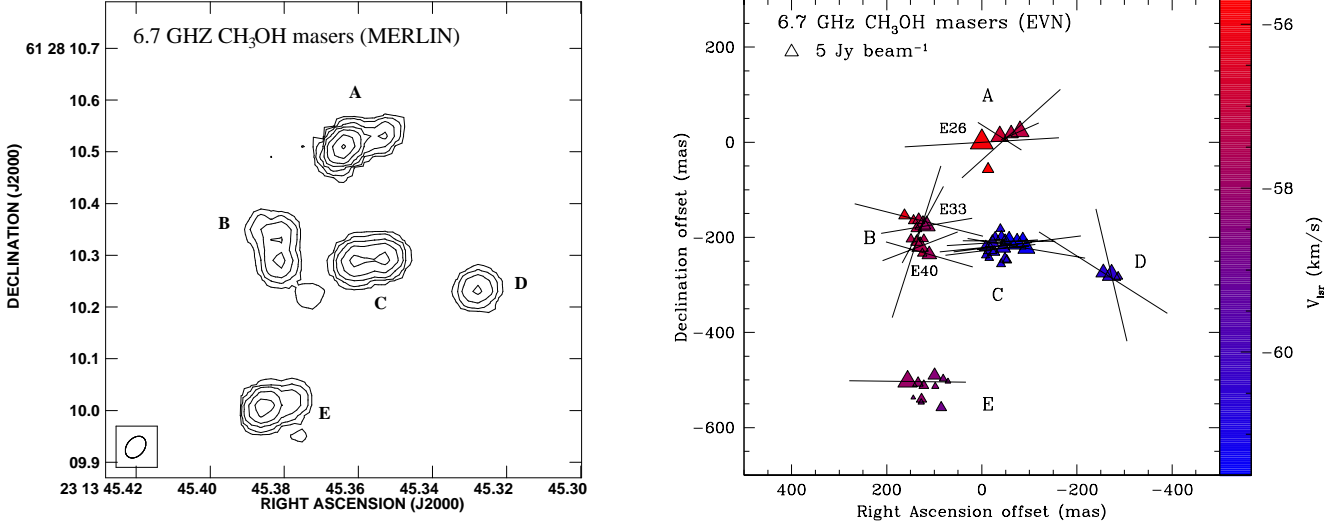


**Fig. 4.** Left panel:  $\text{CH}_3\text{OH}$  maser structures detected with MERLIN around NGC7538-IRS1. Contours are 16, 32, 64, 128, 256, 512,  $1024 \times 0.15 \text{ Jy beam}^{-1}$ . The synthesized beam is  $47 \text{ mas} \times 34 \text{ mas}$ . Right panel: a close-up view of the  $\text{CH}_3\text{OH}$  maser features detected with the EVN around NGC7538-IRS1. The synthesized beam is  $6.3 \text{ mas} \times 4.9 \text{ mas}$ . The triangle symbols are the identified maser features in the present work scaled logarithmically according to their peak flux density. The maser LSR radial velocity is indicated by color. A  $5 \text{ Jy beam}^{-1}$  symbol is plotted for illustration in the right panels. The absolute reference position is  $\alpha_{2000} = 23^{\text{h}}13^{\text{m}}45^{\text{s}}.362$  and  $\delta_{2000} = +61^{\circ}28'10''.506$  as determined from the MERLIN observations. The linear polarization vectors, scaled logarithmically according to the polarization fraction  $P_1$  (Tables 2 and 3), are overplotted.

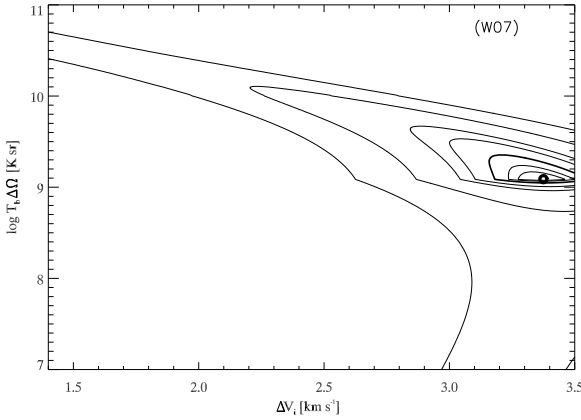


**Fig. 3.** Results of the full radiative transfer  $\chi^2$ -model fits for the  $\text{H}_2\text{O}$  maser feature W07. The fit yields the emerging maser brightness temperature  $T_b \Delta \Omega$  and the intrinsic maser thermal linewidth  $\Delta V_i$ . Contours indicate the significance intervals  $\Delta \chi^2 = 0.25, 0.5, 1, 2, 3, 7$ , with the thick solid contours indicating  $1\sigma$  and  $3\sigma$  areas (see Vlemmings et al. 2006 and Surcis et al. 2011 for more details).

belong to group S (W06 and W07). Their linear polarization fraction (column 7 of Table 1) is  $P_1 \approx 1\%$  and the weighted linear polarization angles is  $\langle \chi_{\text{H}_2\text{O}}^S \rangle \approx -11^\circ$ . The full radiative transfer method code for  $\text{H}_2\text{O}$  masers was able to fit the feature W07 and the results are given in column 10 and 11 of Table 1 and in Fig. 3. The emerging brightness temperature and the intrinsic thermal linewidth are  $10^9 \text{ K sr}$  and  $3.4 \text{ km s}^{-1}$ , respectively. By considering  $T_b \Delta \Omega$  and the observed  $P_1$  we determined  $\theta_{\text{H}_2\text{O}}^B = 81^\circ$ , indicating that the maser is operating in a regime where the magnetic field is close to perpendicular to the propa-

gation of the maser radiation. No significant circular polarization emission is detected.

### 3.2. $\text{CH}_3\text{OH}$ masers

We detected 13 6.7-GHz  $\text{CH}_3\text{OH}$  maser features with the MERLIN telescope (named M01-M13 in Table 2) that appear to be composed of 49 features when observed with the EVN resolution (named E01-E49 in Table 3). Including the more sensitive EVN observations, we detect no  $\text{CH}_3\text{OH}$  maser emission below  $0.1 \text{ Jy beam}^{-1}$ . Note that as defined in Sect. 2, we indicate with the term maser feature the brightest maser spot among a series of maser spots that either show a spatial coincidence and consecutive velocities or show a clear velocity gradient along a continuum linear structure.

In the left panel of Fig. 4 we show the contours of the  $\text{CH}_3\text{OH}$  maser structures detected with MERLIN and in the right panel the distribution of the  $\text{CH}_3\text{OH}$  maser features detected with the EVN. The  $\text{CH}_3\text{OH}$  maser features distribution at high angular resolution match the  $\text{CH}_3\text{OH}$  maser emission detected with MERLIN four years before perfectly. Following the naming convention adopted by Minier et al. (2000), they can be divided into five groups (from A to E). Note that each group is composed of several maser features, each of which indicates a series of maser spots. Group A, which is composed of five maser features (3 at MERLIN resolution) and hosts the brightest maser feature of the region (M06 and E26, respectively), shows a linear distribution. If we consider all maser spots of the maser feature M06 (top-left panel of Fig. 5), we are able to measure a velocity gradient of about  $0.02 \text{ km s}^{-1} \text{ AU}^{-1}$  from northwest to southeast, which is confirmed by considering the matching maser spots of E26 (EVN, top-right panel of Fig. 5).

Group B is resolved into 12  $\text{CH}_3\text{OH}$  maser features (four at MERLIN resolution). The spots of the features E33 and E40



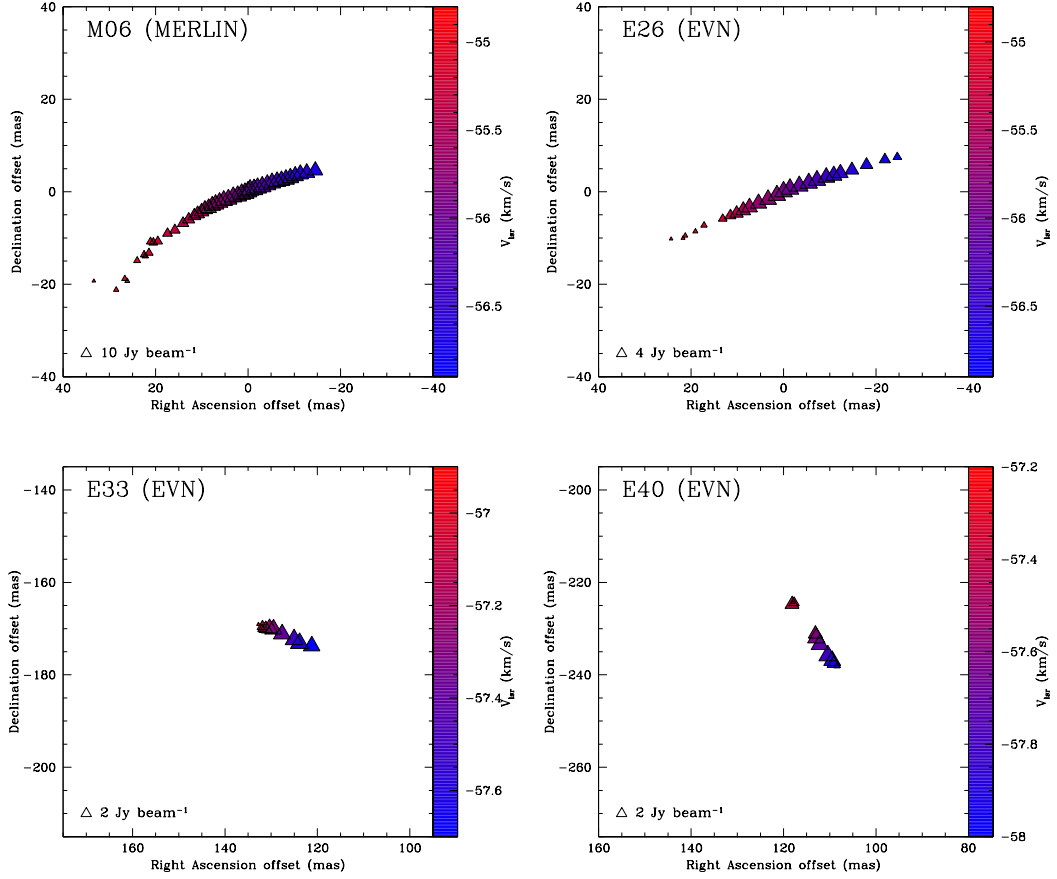


**Fig. 5.** Zoom-in view of the CH<sub>3</sub>OH maser spots of the features M06, which was detected with MERLIN, E26, E33, and E40, which were detected with the EVN. Features M06 and E26 are the same CH<sub>3</sub>OH maser detected with the two instruments. The LSR radial velocity of the spots is indicated by color. Ten, 4, and 2 Jy beam<sup>-1</sup> symbols are plotted for illustration in the panels.

of this group show a velocity gradient similar to that of E26 but from southwest to northeast (bottom panels of Fig. 5). No CH<sub>3</sub>OH maser features of group B detected with MERLIN show a velocity gradient. The CH<sub>3</sub>OH maser groups C, D, and E are composed of 18, 3, and 11 maser features, respectively. While groups C and D are located close to the central peak of the continuum emission, group E is located about 300 mas southward. The velocities of groups C and D are more blue-shifted ( $-61.5 \text{ km s}^{-1} < V_{\text{LSR}} < -60.5 \text{ km s}^{-1}$ ) than those of groups A, B, and E ( $-59 \text{ km s}^{-1} < V_{\text{LSR}} < -56 \text{ km s}^{-1}$ ).

We detected linear polarization in 10 and 20 CH<sub>3</sub>OH maser features with MERLIN and EVN, respectively. The features of group D show the highest linear polarization fraction of the region (column 8 of Tables 2 and 3), though the observations at higher angular resolution revealed E43 to be the feature with the highest linear polarization fraction (6.2%). Because the EVN provides an angular resolution eight times better than MERLIN and because we also have a higher dynamic range, we will, for the interpretation of the magnetic field, only use the linear polarization vectors of the maser features detected with the EVN. The groups A, C, and E have weighted linear polarization vectors almost oriented east-west, with angles  $-86^\circ \pm 31^\circ$ ,  $-88^\circ \pm 6^\circ$ , and  $+89^\circ \pm 44^\circ$ , respectively. The weighted linear polarization angles for the other two groups are  $\langle \chi_{\text{CH}_3\text{OH}}^{\text{B}} \rangle = -60^\circ \pm 36^\circ$  and  $\langle \chi_{\text{CH}_3\text{OH}}^{\text{D}} \rangle = +48^\circ \pm 32^\circ$ .

The full radiative transfer method code for CH<sub>3</sub>OH masers was able to fit 7 (MERLIN) and 20 (EVN) CH<sub>3</sub>OH maser fea-

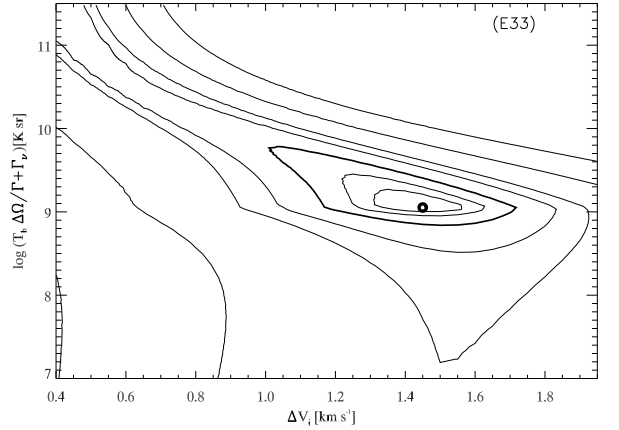


**Fig. 6.** Result of the full radiative transfer  $\chi^2$ -model fits for the CH<sub>3</sub>OH maser E33 detected with the EVN. The fit yields the emerging maser brightness temperature  $T_b \Delta \Omega$  and the intrinsic maser thermal linewidth  $\Delta V_i$ . Contours indicate the significance intervals  $\Delta \chi^2 = 0.25, 0.5, 1, 2, 3, 7$ , with the thick solid contours indicating  $1\sigma$  and  $3\sigma$  areas.

tures, the results are given in columns 10 and 11 of Tables 2 and 3. Considering the high angular resolution observations, the weighted intrinsic maser linewidth and the weighted emerg-

**Table 3.** All 6.7 GHz CH<sub>3</sub>OH maser features detected in NGC7538-IRS 1 with the EVN.

(1)	(2)	(3)	(4)	(5)	(6)	(7)	(8)	(9)	(10)	(11)	(12)	(13)
Maser	group	RA offset (mas)	Dec offset (mas)	Peak flux Density(I) (Jy beam <sup>-1</sup> )	$V_{lsr}$ (km s <sup>-1</sup> )	$\Delta v_L$ (km s <sup>-1</sup> )	$P_l$ (%)	$\chi$ (°)	$\Delta V_i^a$ (km s <sup>-1</sup> )	$T_b \Delta \Omega^a$ (log K sr)	$\Delta V_z^b$ (m s <sup>-1</sup> )	$\theta^c$ (°)
E01	D	-286.910	-282.502	0.55 ± 0.02	-60.40	0.12	—	—	—	—	—	—
E02	D	-272.725	-279.037	16.82 ± 0.03	-60.49	0.21	4.5 ± 0.8	+13 ± 16	1.0 <sup>+0.3</sup> <sub>-0.3</sub>	9.41 <sup>+0.94</sup> <sub>-0.39</sub>	+2.7 ± 0.3	77 <sup>+13</sup> <sub>-11</sub>
E03 <sup>d</sup>	D	-255.344	-273.992	4.72 ± 0.03	-60.58	0.24	5.6 ± 0.9	+58 ± 5	0.9 <sup>+0.3</sup> <sub>-0.1</sub>	9.58 <sup>+0.81</sup> <sub>-0.47</sub>	—	80 <sup>+8</sup> <sub>-10</sub>
E04	C	-93.660	-222.357	10.39 ± 0.02	-61.28	0.24	3.6 ± 0.2	+81 ± 22	1.0 <sup>+0.3</sup> <sub>-0.2</sub>	9.26 <sup>+0.58</sup> <sub>-0.14</sub>	—	83 <sup>+7</sup> <sub>-23</sub>
E05	C	-86.171	-200.790	0.73 ± 0.02	-61.28	0.20	—	—	—	—	—	—
E06	A	-80.377	22.786	15.21 ± 0.03	-57.24	0.20	3.6 ± 0.2	-66 ± 10	1.0 <sup>+0.2</sup> <sub>-0.2</sub>	8.74 <sup>+0.69</sup> <sub>-0.11</sub>	—	87 <sup>+8</sup> <sub>-17</sub>
E07	C	-74.392	-213.730	16.41 ± 0.03	-61.28	0.29	4.1 ± 0.5	-83 ± 20	1.4 <sup>+0.3</sup> <sub>-0.5</sub>	9.39 <sup>+0.92</sup> <sub>-0.25</sub>	—	77 <sup>+8</sup> <sub>-42</sub>
E08	A	-61.547	18.163	4.08 ± 0.02	-57.15	0.23	4.3 ± 1.4	-48 ± 40	0.8 <sup>+0.2</sup> <sub>-0.3</sub>	9.37 <sup>+0.61</sup> <sub>-0.14</sub>	—	79 <sup>+11</sup> <sub>-22</sub>
E09	C	-57.174	-207.658	9.48 ± 0.02	-61.46	0.27	2.5 ± 0.7	-90 ± 4	1.3 <sup>+0.3</sup> <sub>-0.4</sub>	9.10 <sup>+0.84</sup> <sub>-1.25</sub>	—	75 <sup>+15</sup> <sub>-36</sub>
E10	C	-52.938	-248.180	0.73 ± 0.02	-60.84	0.31	—	—	—	—	—	—
E11	C	-49.085	-205.700	1.12 ± 0.03	-60.75	1.08	—	—	—	—	—	—
E12	C	-48.483	-245.093	1.21 ± 0.02	-60.67	0.28	—	—	—	—	—	—
E13	C	-44.930	-222.357	4.65 ± 0.02	-60.84	0.25	1.4 ± 0.4	-86 ± 83	1.2 <sup>+0.3</sup> <sub>-0.3</sub>	8.81 <sup>+0.83</sup> <sub>-1.00</sub>	—	76 <sup>+14</sup> <sub>-38</sub>
E14	C	-41.350	-198.801	1.11 ± 0.01	-61.02	0.49	—	—	—	—	—	—
E15	C	-40.421	-255.891	0.59 ± 0.02	-60.84	0.33	—	—	—	—	—	—
E16	C	-39.082	-181.780	0.57 ± 0.03	-60.75	0.18	—	—	—	—	—	—
E17	A	-37.661	12.650	14.31 ± 0.02	-56.80	0.33	1.4 ± 0.2	+58 ± 12	1.6 <sup>+0.3</sup> <sub>-0.4</sub>	8.77 <sup>+0.75</sup> <sub>-0.25</sub>	—	80 <sup>+10</sup> <sub>-40</sub>
E18	C	-27.986	-199.362	0.80 ± 0.03	-60.75	0.19	—	—	—	—	—	—
E19	C	-25.963	-230.701	1.29 ± 0.02	-60.84	0.26	—	—	—	—	—	—
E20	C	-22.083	-211.354	3.19 ± 0.03	-60.58	0.27	2.4 ± 1.0	-87 ± 23	1.0 <sup>+0.3</sup> <sub>-0.3</sub>	9.05 <sup>+0.39</sup> <sub>-1.86</sub>	—	79 <sup>+11</sup> <sub>-42</sub>
E21	C	-18.147	-226.401	2.53 ± 0.03	-60.75	0.22	2.41 ± 0.04	-83 ± 12	1.0 <sup>+0.3</sup> <sub>-0.2</sub>	9.05 <sup>+0.86</sup> <sub>-0.06</sub>	—	85 <sup>+6</sup> <sub>-41</sub>
E22	C	-15.769	-242.950	0.51 ± 0.02	-60.84	0.25	—	—	—	—	—	—
E23	A	-13.091	-56.523	1.43 ± 0.05	-55.75	0.26	—	—	—	—	—	—
E24	C	-8.172	-220.826	1.83 ± 0.02	-60.67	0.29	2.5 ± 0.3	-84 ± 14	1.3 <sup>+0.3</sup> <sub>-0.4</sub>	9.09 <sup>+0.67</sup> <sub>-0.22</sub>	—	82 <sup>+7</sup> <sub>-39</sub>
E25	C	-7.762	-238.071	0.42 ± 0.02	-60.84	0.32	—	—	—	—	—	—
E26 <sup>d</sup>	A	0	0	95.15 ± 0.05	-55.92	0.33	5.83 ± 0.03	-87 ± 17	0.5 <sup>+0.4</sup> <sub>-0.2</sub>	11.39 <sup>+0.75</sup> <sub>-0.03</sub>	+1.6 ± 0.3	86 <sup>+5</sup> <sub>-19</sub>
E27	E	71.113	-503.039	0.19 ± 0.01	-58.56	0.12	—	—	—	—	—	—
E28	E	81.252	-497.234	0.37 ± 0.01	-58.56	0.27	—	—	—	—	—	—
E29	E	85.297	-557.914	1.06 ± 0.01	-58.91	0.27	—	—	—	—	—	—
E30	E	97.923	-513.329	0.30 ± 0.01	-58.38	0.18	—	—	—	—	—	—
E31	E	99.399	-489.943	2.26 ± 0.01	-58.38	0.21	—	—	—	—	—	—
E32	B	110.386	-235.856	4.37 ± 0.02	-57.77	0.31	2.4 ± 0.6	+74 ± 44	1.4 <sup>+0.3</sup> <sub>-0.4</sub>	9.06 <sup>+0.81</sup> <sub>-1.33</sub>	—	89 <sup>+10</sup> <sub>-38</sub>
E33	B	116.016	-175.760	10.11 ± 0.02	-57.86	0.30	2.5 ± 0.7	-81 ± 83	1.5 <sup>+0.4</sup> <sub>-0.4</sub>	9.05 <sup>+0.94</sup> <sub>-1.28</sub>	—	76 <sup>+15</sup> <sub>-36</sub>
E34	B	121.782	-203.613	0.54 ± 0.02	-57.42	0.55	—	—	—	—	—	—
E35	E	122.083	-511.884	0.80 ± 0.02	-58.21	0.22	—	—	—	—	—	—
E36	B	123.859	-173.165	6.46 ± 0.02	-57.59	0.32	2.3 ± 0.6	-28 ± 42	1.5 <sup>+0.4</sup> <sub>-0.4</sub>	9.04 <sup>+1.00</sup> <sub>-1.08</sub>	—	89 <sup>+12</sup> <sub>-38</sub>
E37	B	125.062	-233.976	0.68 ± 0.02	-57.07	0.28	—	—	—	—	—	—
E38	E	126.893	-540.110	0.93 ± 0.03	-58.12	0.21	—	—	—	—	—	—
E39	E	127.303	-546.631	0.21 ± 0.06	-58.73	0.26	—	—	—	—	—	—
E40	B	129.927	-218.961	8.98 ± 0.02	-57.51	0.37	2.1 ± 0.7	-69 ± 10	1.8 <sup>+0.1</sup> <sub>-0.4</sub>	8.99 <sup>+1.00</sup> <sub>-1.15</sub>	—	71 <sup>+9</sup> <sub>-44</sub>
E41 <sup>d</sup>	B	132.550	-163.392	1.81 ± 0.02	-57.24	0.34	4.3 ± 1.1	+76 ± 42	0.6 <sup>+0.5</sup> <sub>-0.1</sub>	9.44 <sup>+0.30</sup> <sub>-1.72</sub>	—	85 <sup>+3</sup> <sub>-17</sub>
E42	E	134.190	-506.261	1.10 ± 0.03	-58.12	0.20	—	—	—	—	—	—
E43 <sup>d</sup>	B	137.196	-209.274	1.69 ± 0.03	-57.24	0.37	6.2 ± 2.0	-18 ± 17	0.5 <sup>+0.3</sup> <sub>-0.3</sub>	9.83 <sup>+0.22</sup> <sub>-1.94</sub>	—	90 <sup>+20</sup> <sub>-20</sub>
E44	B	137.552	-181.682	1.05 ± 0.02	-57.33	0.24	—	—	—	—	—	—
E45	B	143.509	-164.852	0.98 ± 0.02	-56.72	0.32	—	—	—	—	—	—
E46	E	144.083	-537.047	0.12 ± 0.01	-58.73	0.28	—	—	—	—	—	—
E47	B	149.112	-203.584	0.71 ± 0.02	-57.42	0.27	—	—	—	—	—	—
E48	E	156.163	-503.223	23.68 ± 0.03	-58.03	0.24	3.5 ± 0.6	+89 ± 44	1.2 <sup>+0.2</sup> <sub>-0.4</sub>	9.26 <sup>+1.00</sup> <sub>-0.31</sub>	-2.7 ± 0.3	75 <sup>+15</sup> <sub>-35</sub>
E49	B	162.558	-154.095	1.50 ± 0.05	-56.19	0.16	—	—	—	—	—	—

**Notes.** <sup>(a)</sup> The best-fitting results obtained by using a model based on the radiative transfer theory of CH<sub>3</sub>OH masers for  $\Gamma + \Gamma_v = 1\text{ s}^{-1}$  (Vlemmings et al. 2010). The errors were determined by analyzing the full probability distribution function. For  $\Gamma + \Gamma_v = 0.6\text{ s}^{-1}$  (Minier et al. 2002)  $T_b \Delta \Omega$  has to be adjusted by adding  $-0.22$ . <sup>(b)</sup> The Zeeman-splittings are determined from the cross-correlation between the RR and LL spectra. <sup>(c)</sup> The angle between the magnetic field and the maser propagation direction is determined by using the observed  $P_l$  and the fitted emerging brightness temperature. The errors were determined by analyzing the full probability distribution function. <sup>(d)</sup> Because of the degree of the saturation of these H<sub>2</sub>O masers,  $T_b \Delta \Omega$  is underestimated,  $\Delta V_i$  and  $\theta$  are overestimated.

**Table 4.** Weighted values of the linear polarization angles, the intrinsic thermal linewidths, the emerging brightness temperatures, and the angles between the line of sight and the magnetic field of the CH<sub>3</sub>OH masers for feature in common.

Group	EVN				MERLIN			
	$\langle \chi \rangle$ (°)	$\langle \Delta V_i \rangle$ (km s <sup>-1</sup> )	$\langle T_b \Delta \Omega \rangle$ (K sr)	$\langle \theta \rangle$ (°)	$\langle \chi \rangle$ (°)	$\langle \Delta V_i \rangle$ (km s <sup>-1</sup> )	$\langle T_b \Delta \Omega \rangle$ (K sr)	$\langle \theta \rangle$ (°)
A	-86 ± 31	0.9 <sup>+0.4</sup> <sub>-0.3</sub>	5 × 10 <sup>9</sup>	86 <sup>+4</sup> <sub>-2</sub>	-51 ± 62	<1.2 <sup>a</sup>	> 5 × 10 <sup>8b</sup>	90 <sup>+33</sup> <sub>-53</sub>
B	-60 ± 36	0.5 <sup>+0.9</sup> <sub>-0.3</sub>	1 × 10 <sup>9</sup>	87 <sup>+4</sup> <sub>-2</sub>	-63 ± 76	<0.9 <sup>a</sup>	> 1 × 10 <sup>12b</sup>	-
C	-88 ± 6	1.0 <sup>+0.1</sup> <sub>-0.4</sub>	2 × 10 <sup>9</sup>	85 <sup>+4</sup> <sub>-6</sub>	-74 ± 69	2.2 <sup>+0.1</sup> <sub>-0.1</sub>	3 × 10 <sup>8</sup>	76 <sup>+11</sup> <sub>-46</sub>
D	+48 ± 32	0.6 <sup>+0.4</sup> <sub>-0.1</sub>	2 × 10 <sup>10</sup>	79 <sup>+8</sup> <sub>-13</sub>	+39 ± 8	<0.6 <sup>a</sup>	> 1 × 10 <sup>12b</sup>	-
E	+89 ± 44	1.2 <sup>+0.2</sup> <sub>-0.4</sub>	2 × 10 <sup>9</sup>	75 <sup>+15</sup> <sub>-35</sub>	+21 ± 54	1.5 <sup>+0.1</sup> <sub>-0.1</sub>	6 × 10 <sup>8</sup>	86 <sup>+5</sup> <sub>-29</sub>

**Notes.** <sup>(a)</sup> Only the highest value has been taken into account. <sup>(b)</sup> Only the lowest value has been taken into account.

ing brightness temperature are  $\langle \Delta V_i \rangle_{\text{CH}_3\text{OH}} = 0.9\text{ km s}^{-1}$  and  $\langle T_b \Delta \Omega \rangle_{\text{CH}_3\text{OH}} \approx 10^9\text{ K sr}$ . As an example, the  $\chi^2$ -contours for feature E33 are reported in Fig. 6.

The fit for the CH<sub>3</sub>OH maser features detected with MERLIN gives values both for  $\Delta V_i$  and for  $T_b \Delta \Omega$  consistent or higher than those detected with the EVN (see Table 4). However, owing to the lower angular resolution of MERLIN and the occur-



rence of strong velocity gradients, the fits are strongly affected by line blending. As for the  $\text{H}_2\text{O}$  maser features, we are able to determine the  $\theta$  values (column 12 and 13 of Tables 2 and 3, respectively) from  $T_b\Delta\Omega$  and  $P_1$ . The weighted value for the whole region is  $\langle\theta_{\text{CH}_3\text{OH}}\rangle_{\text{EVN}} = 86^{+4}_{-43}^\circ$ , which is almost constant in all groups. Only for group E we determine a lower value, i.e.,  $\langle\theta_{\text{CH}_3\text{OH}}^{\text{E}}\rangle_{\text{EVN}} = 75^{+15}_{-35}^\circ$ .

The Zeeman-splitting ( $\Delta V_Z$ ) in  $\text{m s}^{-1}$  determined from the cross-correlation between the RR and LL spectra of the  $\text{CH}_3\text{OH}$  maser features detected with the EVN is reported in column 12 of Table 3. Note that the cross-correlation method is dynamic-range sensitive, therefore we are able to measure  $\Delta V_Z$  only for those features that show a very high dynamic range. It has been impossible to obtain  $\Delta V_Z$  measurements from MERLIN data because of the insufficient dynamic range.

## 4. Discussion

### 4.1. Comparing $\text{CH}_3\text{OH}$ spectra at different resolution

Vlemmings (2008) observed the  $\text{CH}_3\text{OH}$  masers with the 100-m Effelsberg telescope in November 2007, i.e. two years later than our MERLIN observations and two years before our EVN observations. A comparison between the single-dish and MERLIN fluxes reveals only a difference of  $\leq 10\%$  across the whole spectra. This slight difference can be explained by the different resolution of the two instruments and flux calibration uncertainties in the Effelsberg observations ( $\sim 10\%$ , Vlemmings 2008). This means that no significant changes occurred between the two epochs and there is no indication of a core/halo structure of the maser features (hereafter simply called masers) at scales of  $\sim 100$  AU such as described for a sample of  $\text{CH}_3\text{OH}$  maser sources by Pandian et al. (2011).

In Fig. 7 we show the total flux spectra of the

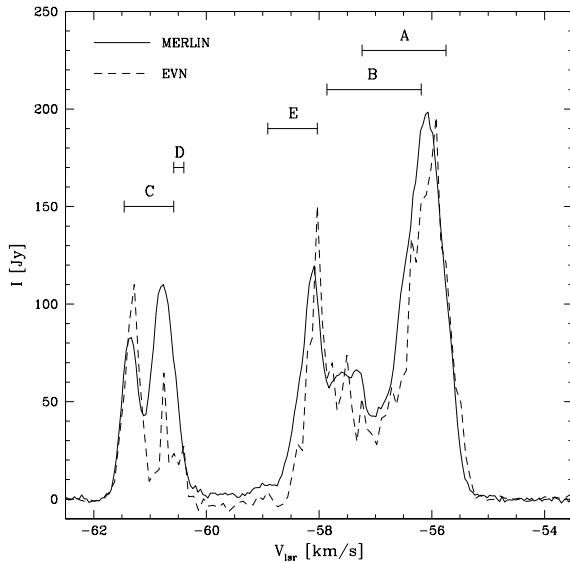


**Fig. 7.** Profile of the total flux spectra of the  $\text{CH}_3\text{OH}$  masers in NGC7538 detected with MERLIN (solid line, epoch 2005) and the EVN (dashed line, epoch 2009). The groups are also reported according to the velocity of Table 3.

$\text{CH}_3\text{OH}$  masers detected with MERLIN and the EVN in 2005 and 2009, respectively. Generally, the EVN resolved out between 60% and 90% of the flux when 6.7-GHz  $\text{CH}_3\text{OH}$  masers

were observed with both these instruments (e.g., Minier et al. 2002; Bartkiewicz et al. 2009; Torstensson et al. 2011). This indicates the presence of emission structures on scales that are resolved by the EVN, i.e. a halo structure that surrounds the core of the masers. Moreover, if the maser spots do not have a compact core, they would not be detected in the EVN observations (Pandian et al. 2011). Although in our observations the EVN resolves out about 50% of the flux of group C ( $V_{\text{lsr}} > -61 \text{ km s}^{-1}$ ), the majority of the flux appears to be recovered across the entire  $\text{CH}_3\text{OH}$  maser spectrum. This suggests that the halo structure is absent, except in some masers of group C and likely in E26 of group A, and that the masers only contain a compact core. Moreover, the non-detection of the maser M07 with the EVN might indicate the absence of the compact core in this maser.

Minier et al. (2002) observed the 6.7-GHz  $\text{CH}_3\text{OH}$  masers with five antennas of the EVN. The authors determined the size of the halo ( $d_1$ ) and of the core ( $d_2$ ) of the brightest masers of groups A and C by Gaussian fitting of the visibility amplitudes. For the brightest maser of group A the authors determined  $d_1 = 5 \text{ mas}$  ( $\sim 13 \text{ AU}$  at 2.65 kpc) and  $d_2 = 3 \text{ mas}$  ( $\sim 8 \text{ AU}$ ), and  $d_1 = 17 \text{ mas}$  ( $\sim 45 \text{ AU}$ ), and  $d_2 = 5 \text{ mas}$  ( $\sim 13 \text{ AU}$ ) were measured for the brightest maser of group C. The Gaussian fit of E26 and E07 gives a size of 5 mas and 6 mas respectively, indicating that the EVN resolves out the halo structure observed by Minier et al. (2002) and that we observe only the core of these two masers.

We suggest that the absence of a halo structure in most of the  $\text{CH}_3\text{OH}$  masers could be caused by the amplification of the strong continuum emission shown in Fig. 1. This would argue that almost all  $\text{CH}_3\text{OH}$  masers are on the front-side of this source. Similar arguments were used in the interpretation of the structure of Cepheus A (Torstensson et al. 2011).

### 4.2. $\text{H}_2\text{O}$ and $\text{CH}_3\text{OH}$ maser properties

Before discussing the polarization analysis of the masers in NGC7538-IRS1, we need to consider the degree of the maser saturation. As explained in detail by Vlemmings et al. (2010) and Surcis et al. (2011), when the full radiative transfer method code is applied to a saturated maser, the code gives a lower limit for  $T_b\Delta\Omega$  and an upper limit for  $\Delta V_i$ . The masers are unsaturated when  $R/(\Gamma + \Gamma_v) < 1$  and fully saturated when  $R/(\Gamma + \Gamma_v) \sim 100$ , where  $R$  is the stimulated emission rate given by

$$R \simeq \frac{Ak_B T_b \Delta\Omega}{4\pi h\nu}. \quad (1)$$

Here  $A$  is the Einstein coefficient for the maser transition, which for  $\text{H}_2\text{O}$  masers is taken to be equal to  $2 \times 10^9 \text{ s}^{-1}$  (Goldreich & Keeley 1972) and for the  $\text{CH}_3\text{OH}$  masers is  $0.1532 \times 10^8 \text{ s}^{-1}$  (Vlemmings et al. 2010),  $k_B$  and  $h$  are the Boltzmann and Planck constants, respectively, and  $\nu$  the maser frequency. From  $R/(\Gamma + \Gamma_v) < 1$  we can estimate an upper limit for the emerging brightness temperature below which the masers can be considered unsaturated. The limits are  $(T_b\Delta\Omega)_{\text{H}_2\text{O}} < 6.7 \times 10^9 \text{ K sr}$  and  $(T_b\Delta\Omega)_{\text{CH}_3\text{OH}} < 2.6 \times 10^9 \text{ K sr}$  for  $\text{H}_2\text{O}$  and  $\text{CH}_3\text{OH}$  masers, respectively. Consequently, only four  $\text{CH}_3\text{OH}$  masers are partly saturated; i.e., E03, E26, E41 and E43 (Table 3). Because the model emerging brightness temperature scales linearly with  $\Gamma + \Gamma_v$ , the ratio  $R/(\Gamma + \Gamma_v)$  is independent of the value of  $\Gamma + \Gamma_v$ . The  $\Delta v_L$  of the saturated  $\text{CH}_3\text{OH}$  masers are close to  $\Delta V_i$  implying that the maser lines are rebroadened as expected when the maser becomes saturated. Furthermore, these four  $\text{CH}_3\text{OH}$  masers do also show a high linear polarization fraction, which again confirms their saturated state (Goldreich et al. 1973).

The intrinsic linewidth of the H<sub>2</sub>O maser W07 is higher than the typical values measured in previous works, i.e.  $\Delta V_i = 2.5 \text{ km s}^{-1}$  (Surcis et al. 2011). This difference might indicate the presence of a strong turbulent gas with a turbulence velocity of  $\Delta V_{\text{turb}} = 2.3 \text{ km s}^{-1}$  or multiple components overlapping.

By comparing the brightness temperature  $T_b$  with  $T_b \Delta \Omega$  obtained from the model, we can estimate the maser beaming angle ( $\Delta \Omega$ ) for both maser species. We can estimate the brightness temperature ( $T_b$ ) by considering the equation

$$\frac{T_b}{[\text{K}]} = \frac{S(\nu)}{[\text{Jy}]} \cdot \left( \frac{\Sigma^2}{[\text{mas}^2]} \right)^{-1} \cdot \xi, \quad (2)$$

where  $S(\nu)$  is the flux density,  $\Sigma$  the maser angular size and  $\xi$  is a constant factor that includes all constant values, such as the Boltzmann constant, the wavelength, and the proportionality factor obtained for a Gaussian shape by Burns et al. (1979). The values of  $\xi$  for H<sub>2</sub>O and CH<sub>3</sub>OH masers are

$$\xi_{22 \text{ GHz}} = 1.24 \cdot 10^9 \text{ mas}^2 \text{ Jy}^{-1} \text{ K}, \quad (3)$$

$$\xi_{6.7 \text{ GHz}} = 13.63 \cdot 10^9 \text{ mas}^2 \text{ Jy}^{-1} \text{ K}, \quad (4)$$

as reported by Surcis et al. (2011) and Surcis et al. (2009), respectively. The H<sub>2</sub>O maser W07 is unresolved and  $\Delta \Omega_{\text{H}_2\text{O}} = 10^{-2}$ . The Gaussian fit of CH<sub>3</sub>OH masers detected with the EVN gives a size between 5 and 7 mas, which indicates that all CH<sub>3</sub>OH masers are marginally resolved.

In a tubular geometry  $\Delta \Omega \approx (d/l)^2$ , where  $d$  and  $l$  are the transverse size and length of the tube, respectively. By assuming  $d$  approximately the size of the masers, the maser lengths are in the range  $10^{13} \text{ cm} < l_{\text{H}_2\text{O}} < 10^{14} \text{ cm}$  and  $10^{14} \text{ cm} < l_{\text{CH}_3\text{OH}} < 10^{15} \text{ cm}$  for W07 and the CH<sub>3</sub>OH masers, respectively.

### 4.3. Magnetic field in NGC7538-IRS 1

#### 4.3.1. CH<sub>3</sub>OH Zeeman-splitting and magnetic field

We measured 6.7-GHz CH<sub>3</sub>OH maser Zeeman-splitting ranging from  $-2.7 \text{ m s}^{-1}$  to  $+2.7 \text{ m s}^{-1}$ . This is 2–3 times larger than was measured with the Effelsberg telescope (Vlemmings 2008) as expected when resolving individual masers. From the Zeeman theory we know that the Zeeman-splitting is related to the magnetic field strength along the line of sight ( $B_{\parallel}$ ) by the equation

$$\Delta V_Z = \alpha_Z \cdot B_{\parallel}, \quad (5)$$

where  $\Delta V_Z$  is the Zeeman-splitting in  $\text{km s}^{-1}$  and  $\alpha_Z$  is the Zeeman-splitting coefficient in  $\text{km s}^{-1} \text{ G}^{-1}$ , which strongly depends on the Landé  $g$ -factor of the molecular transition. Recently, Vlemmings et al. (2011) found an unfortunate calculation error in the  $\alpha_Z$  used so far ( $\alpha_Z = 0.049 \text{ km s}^{-1} \text{ G}^{-1}$ ; e.g., Surcis et al. 2009, Vlemmings et al. 2010), the current best value is found to be one order of magnitude lower ( $\alpha_Z = 0.005 \text{ km s}^{-1} \text{ G}^{-1}$ ). However, Vlemmings et al. (2011) show that the splitting between the RCP- and LCP-signal still likely originates from the Zeeman theory and not from other non-Zeeman effects. Until careful laboratory measurements of the  $g$ -factor appropriate for the 6.7-GHz CH<sub>3</sub>OH masers are made, we cannot give any exact value for the magnetic field strength. Because there is a linear proportionality between  $\Delta V_Z$  and  $B_{\parallel}$ , we can say that the negative value of the Zeeman-splitting indicates a magnetic field oriented toward the observer and positive away from the observer. However, we can speculatively give a possible range of values for  $|B_{\parallel}|$  by considering  $0.005 \text{ km s}^{-1} \text{ G}^{-1} < \alpha_Z < 0.049 \text{ km s}^{-1} \text{ G}^{-1}$ , thus  $50 \text{ mG} \lesssim |B_{\parallel}| \lesssim 500 \text{ mG}$ .

#### 4.3.2. Magnetic field orientation

Before discussing the orientation of the magnetic field, we have to evaluate the foreground Faraday rotation (i.e., the rotation caused by the medium between the source and the observer), which is given by

$$\Phi_f [^\circ] = 4.22 \times 10^6 \left( \frac{D}{[\text{kpc}]} \right) \left( \frac{n_e}{[\text{cm}^{-3}]} \right) \left( \frac{B_{\parallel}}{[\text{mG}]} \right) \left( \frac{\nu}{[\text{GHz}]} \right)^{-2}, \quad (6)$$

where  $D$  is the length of the path over which the Faraday rotation occurs,  $n_e$  and  $B_{\parallel}$  are respectively the average electron density and the magnetic field along this path and  $\nu$  is the frequency. By assuming the interstellar electron density, the magnetic field, and the distance are  $n_e \approx 0.012 \text{ cm}^{-3}$ ,  $B_{\parallel} \approx 2 \mu\text{G}$  (Sun et al. 2008), and  $D = 2.65 \text{ kpc}$ , respectively,  $\Phi_f$  is estimated to be  $0.5^\circ$  at 22-GHz and  $6.0^\circ$  at 6.7-GHz. At both frequencies the foreground Faraday rotation is within the errors reported in Tables 1 and 3 thus it should not affect our conclusions.

Because all  $\theta$  values are higher than the Van Vleck angle  $\theta_{\text{crit}} \sim 55^\circ$  (Goldreich et al. 1973), the magnetic fields are inferred to be perpendicular to the linear polarization vectors. The magnetic field orientation derived from the H<sub>2</sub>O masers is  $\varphi_{\text{H}_2\text{O}} = +79^\circ$ , while the five groups of CH<sub>3</sub>OH masers show orientation angles  $\varphi_{\text{CH}_3\text{OH}}^A = +4^\circ$ ,  $\varphi_{\text{CH}_3\text{OH}}^B = +30^\circ$ ,  $\varphi_{\text{CH}_3\text{OH}}^C = +2^\circ$ ,  $\varphi_{\text{CH}_3\text{OH}}^D = -42^\circ$ , and  $\varphi_{\text{CH}_3\text{OH}}^E = -1^\circ$ . However, considering the relatively large errors in column 13 of Table 3, we cannot rule out that the actual  $\theta$  values are below  $55^\circ$ , in which case the magnetic field is parallel to the linear polarization vectors.

Because Hutawarakorn & Cohen (2003) measured the linear polarized emission of the 1.6 and 1.7-GHz OH masers, we can now compare the orientation of the magnetic field derived from the two maser species (Fig. 1). We have to consider that the Faraday rotation at the OH maser frequencies is, at the same conditions, larger than at 6.7-GHz. The linear polarization angles of group D show a  $90^\circ$  difference w.r.t those of the nearby 1.6-GHz OH masers. This might be caused either by a  $90^\circ$ -flip phenomenon or by the Faraday rotation if the masers are deeply located in a strong ionized gas. Most of the OH masers are likely to be Zeeman  $\sigma$ -components, therefore the magnetic field is perpendicular to the linear polarization vectors. Considering the large errors of  $\theta_{\text{E48}}$ , the orientation of the magnetic fields of group B and E are consistent with those derived from the nearby 1.6-GHz OH masers (Hutawarakorn & Cohen 2003). In particular, the linear polarization vector of E43, which shows the highest linear polarization fraction, is perfectly aligned with feature 2 of the 1665 MHz OH maser (Hutawarakorn & Cohen 2003). Unless the Faraday rotation is  $180^\circ$ , the consistence of the magnetic field orientation indicates that the Faraday rotation at OH maser frequency is low.

#### 4.3.3. The role of the magnetic field

The importance of the magnetic field in the region can be estimated by evaluating the ratio between thermal and magnetic energies ( $\beta$ ). If  $\beta < 1$ , the magnetic field dominates the energies in the high-density protostellar environment. The  $\beta$  factor is given by

$$\beta = 2 \left( \frac{m_a}{m_s} \right)^2, \quad (7)$$

where  $m_a$  is the Alfvénic Mach number and  $m_s$  is the sonic Mach number, which in formula are

$$m_a = \frac{\sigma \sqrt{3}}{V_A}, \quad \text{and} \quad m_s = \frac{\sigma \sqrt{3}}{c_s}. \quad (8)$$

Here  $V_A$  is the Alfvén velocity and  $c_s$  is the sound velocity, and  $\sigma$ , the turbulence velocity, can be estimated using  $\sigma = \Delta V_{\text{turb}} / \sqrt{8 \ln 2}$ . By considering a mass  $\mu_{\text{H}_2} = 3.8 \times 10^{-24}$  g and the relation between the velocity and the temperature of a gas, we can write  $V_A$  and  $c_s$  in terms of  $|B|$ ,  $n_{\text{H}_2}$ , and the kinetic temperature of the gas  $T_k$

$$\frac{V_A}{[\text{km s}^{-1}]} = 1542 \left( \frac{|B|}{[\text{mG}]} \right) \left( \frac{n_{\text{H}_2}}{[\text{cm}^{-3}]} \right)^{-\frac{1}{2}}, \quad (9)$$

$$\frac{c_s}{[\text{km s}^{-1}]} = 0.0603 \left( \frac{T_k}{[\text{K}]} \right)^{-\frac{1}{2}}. \quad (10)$$

So we get

$$\beta = 3.058 \cdot 10^{-9} \left( \frac{|B|}{[\text{mG}]} \right)^{-2} \left( \frac{n_{\text{H}_2}}{[\text{cm}^{-3}]} \right) \left( \frac{T_k}{[\text{K}]} \right), \quad (11)$$

which, considering Eq. 5 and  $|B| = |B_{\parallel}| / \cos \langle \theta \rangle$ , can thus be written as

$$\beta = 3.058 \cdot 10^{-9} \alpha_Z^2 \cos \langle \theta \rangle \left( \frac{|\Delta V_Z|}{[\text{ms}^{-1}]} \right)^{-2} \left( \frac{n_{\text{H}_2}}{[\text{cm}^{-3}]} \right) \left( \frac{T_k}{[\text{K}]} \right). \quad (12)$$

By assuming  $n_{\text{H}_2} = 10^9 \text{ cm}^{-3}$ ,  $T \sim 200 \text{ K}$ , which are the typical values in the  $\text{CH}_3\text{OH}$  masing region, the weighted values for the unsaturated masers of the  $\theta$  angle  $\langle \theta \rangle = 78^\circ$ , and Zeeman splittings  $|\Delta V_Z| = 2.7 \text{ m s}^{-1}$ , we obtain

$$\beta = 17.4 \cdot \alpha_Z^2. \quad (13)$$

Although the value of  $\alpha_Z$  is still uncertain, we can expect that this must be neither higher than the old value ( $\alpha_Z = 0.049 \text{ km s}^{-1} \text{ G}^{-1}$ , Vlemmings 2008) nor lower than the new value ( $\alpha_Z = 0.005 \text{ km s}^{-1} \text{ G}^{-1}$ , Vlemmings et al. 2011). Therefore, it is reasonable that  $\beta$  is between  $4 \cdot 10^{-4}$  and  $4 \cdot 10^{-2}$ . Consequently the magnetic field is dynamically important in this massive star-forming region.

#### 4.4. Structure of NGC7538-IRS 1

Recently, large-scale elliptical configurations have been detected in significant  $\text{CH}_3\text{OH}$  masers around high-mass proto-stars. These masers are thought to trace molecular rings (e.g., Bartkiewicz et al. 2009). However, most of these rings do not show signs of rotation, but instead the radial motions dominate, indicating that the masers are instead tracing infalling gas in the interface between the torus and the flow, e.g. Cepheus A HW2 (Torstensson et al. 2011; Vlemmings et al. 2010). In this light it is legitimate to reconsider whether the masers in NGC7538-IRS 1 could trace similar gas.

In this work we have observed velocity gradients in three  $\text{CH}_3\text{OH}$  masers, i.e., E26, E33, and E40. Whereas the velocity gradient of E26 has already been observed by other authors (e.g., Minier et al. 1998; Pestalozzi et al. 2004), those of masers E33 and E40 have not been reported so far (Fig. 5). All velocity gradients of E26, E33, and E40 are equal to  $0.02 \text{ km s}^{-1} \text{ AU}^{-1}$ . Considering the orientation of the linear distribution of the maser spots of E26, E33, and E40, we find that all of them seem to point

toward a common center. This suggests that E26, E33, and E40 are likely tracing a gas with a radial motion, probably consistent with the interface of the torus and infalling gas. Consequently the maser spots of E26 are likely not tracing a Keplerian disk as proposed by Pestalozzi et al. (2004). The  $\text{CH}_3\text{OH}$  masers of groups A, B, C, and D show a cone-shape distribution that opens to the north-west. This seems to indicate that we are looking at a regular structure, for instance the inner part of a torus. Klaassen et al. (2009) detected an almost face-on 5300 AU-torus perpendicular to the outflow with a clockwise rotation motion. If this torus is on the same plane of the disk supposed by De Buizer & Minier (2005), then its inclination angle must be  $i=32^\circ$ . By keeping in mind these new results, we can suppose that the  $\text{CH}_3\text{OH}$  masers of groups A, B, and C are tracing the surface of the inner torus, possibly where the infall reaches the rotating structure. The masers of groups D and E trace the gas slightly farther out on the torus. In particular, group A is located to the opposite side of the torus w.r.t. the other three maser groups. In Fig. 8 a three-dimensional sketch of the region as described above is shown. The outflow sketched here is a simplified representation of the chaotic and complex multi-outflows structure observed toward NGC7538 and in particular around IRS-1 (e.g., Qiu et al. 2011; Klaassen et al. 2011).

In this scenario the  $\text{H}_2\text{O}$  masers of group N are located parallel to the edges of the outflow, which show a blue-shifted part northwestern and a red-shifted part southeastern (e.g., Kameya et al. 1989; Hutawarakorn & Cohen 2003). In this case the  $\text{H}_2\text{O}$  masers can be pumped by a shock caused by the interaction of the outflow with the infalling gas. The most southern  $\text{H}_2\text{O}$  masers, W06 and W07, might be associated either with the red-shifted part of the outflow or most likely with another source, as also suggested by the different orientation of the magnetic field in that region. Moreover, the OH masers located southward (Hutawarakorn & Cohen 2003) might be pumped by the red-shifted part of the high-velocity outflow and those located westward by the blue-shifted part.

This scenario is further supported by the similarity between the torus and outflow velocities and that of the three maser species. In Fig. 9 we plot the  $\text{CH}_3\text{OH}$  maser velocities as a function of the position angle (PA) along the torus. To determine the PA of each individual  $\text{CH}_3\text{OH}$  maser, we consider that every maser lies on an own circle that has the same orientation and inclination angle of the torus with the center located at the origin of the sketched outflow in Fig 8. Moreover, we plot in Fig. 9 an empirical function (solid line) based on the orientation and on the velocity field of the torus observed by Klaassen et al. (2009), i.e. the PA and velocity of all the points of a circle that has the same size, orientation, and inclination of the torus. The maser velocities perfectly match the non-Keplerian velocity profile of the torus that is rotating clockwise (Klaassen et al. 2009). This indicates that the  $\text{CH}_3\text{OH}$  masers are likely related to the torus structure. Groups A and E appear to be systematically blue- and red-shifted w.r.t the torus velocities respectively, supporting the suggestion of infall motion (on the order of  $1 \text{ km s}^{-1}$ ) along the line of sight.

The velocities of the blue- and red-shifted part of the outflow are  $V_{\text{outf}}^{\text{blue}} = -76 \text{ km s}^{-1}$  and  $V_{\text{outf}}^{\text{red}} = -37 \text{ km s}^{-1}$  (Kameya et al. 1989). The mean velocities of the  $\text{H}_2\text{O}$  masers of group N and S are  $V_{\text{H}_2\text{O}}^{\text{N}} = -59.4 \text{ km s}^{-1}$ , excluding the masers W16 and W17, and  $V_{\text{H}_2\text{O}}^{\text{S}} = -68.7 \text{ km s}^{-1}$ . While  $V_{\text{H}_2\text{O}}^{\text{S}}$  again suggests that these masers might be associated with another source, the difference between  $V_{\text{H}_2\text{O}}^{\text{N}}$  and  $V_{\text{outf}}^{\text{blue}}$  indicates that the  $\text{H}_2\text{O}$  masers are tracing the gas surrounding and being entrained by the outflow. The

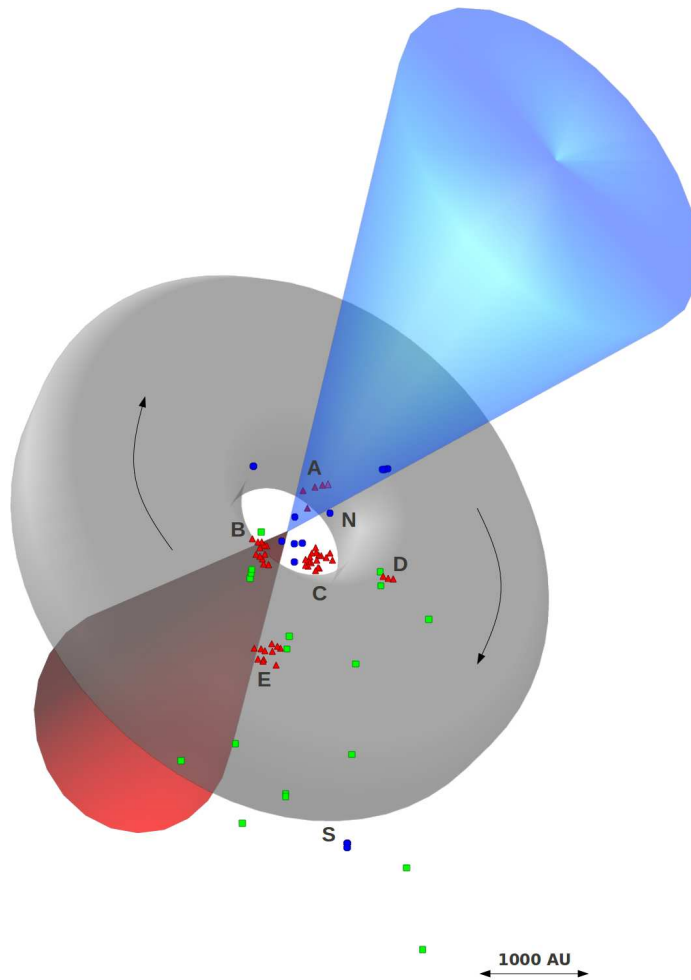


**Fig. 8.** The three-dimensional sketch of the massive star-forming region NGC7538-IRS 1 as described in Sect. 4.4. The two cones are the red- and blue-shifted part of the large-scale molecular bipolar outflow (Kameya et al. 1989), the donut is the torus suggested by Klaassen et al. (2009) perpendicular to the outflow and with  $i=32^\circ$  (De Buizer & Minier 2005), the triangles, the circles, and the boxes are the methanol,  $\text{H}_2\text{O}$  masers (present paper), and the OH masers (Hutawarakorn and Cohen 2003), respectively. The outflow and the torus are transparent to allow the reader to see behind them.

1.6 and 1.7-GHz OH masers show velocity ranges  $-61 \text{ km s}^{-1} < V_{\text{OH}} < -51 \text{ km s}^{-1}$  that agree well with  $V_{\text{torus}}$  and  $V_{\text{CH}_3\text{OH}}$ , which might indicate an association with the torus rather than with the CO-outflow. The presence of OH and  $\text{CH}_3\text{OH}$  masers in the same environments, also suggested by the linear polarization vectors of the two maser species (see Sect. 4.3.2), is in contrast with the excitation model of Cragg et al. (2002), which predicts the inhibition of the 6.7-GHz  $\text{CH}_3\text{OH}$  masers when 1.6-GHz OH masers arise.

The orientation of the magnetic field derived by the linear polarized emission of the  $\text{CH}_3\text{OH}$  masers at high angular resolution matches the scenario we presented above. Most likely the magnetic field is perpendicular to the linear polarization vectors for most of the  $\text{CH}_3\text{OH}$  maser features, but for group E the magnetic field is instead parallel to the linear polarization vectors (see Sect. 4.3.1). This is also suggested by considering the linear polarization vectors of the OH masers (see Sect. 4.3.2). In this case the magnetic field is situated on the two surfaces of the torus, with a counterclockwise direction on the top surface. This interpretation is consistent with the signs of the magnetic field strengths determined from the Zeeman-splitting measure-

ments of the  $\text{CH}_3\text{OH}$  masers and OH masers, which show negative strength ( $B = -2.0 \text{ mG}$ , Hutawarakorn & Cohen 2003) toward the region where groups B and E arise and positive toward groups A and D.

Even if the  $\text{CH}_3\text{OH}$  masers are not tracing the Keplerian-disk reported by Pestalozzi et al. (2004), the presence of a smaller disk is not ruled out. In the scenario proposed here, it would be located within the torus. Accordingly, we argue that a possible answer to the question about the morphology of NGC7538-IRS 1 is that the  $\text{CH}_3\text{OH}$  masers are tracing a gas close to the torus that is falling toward the connection region between the torus and the disk as was observed in other protostars (e.g., Vlemmings et al. 2010).

The new scenario described in this paper is determined by considering the entire  $\text{CH}_3\text{OH}$  maser region and not just the masers of group A. Consequently, this scenario is different both from “Scenario A” and from “Scenario B” suggested by Kraus et al. (2006), who considered the results obtained by De Buizer & Minier (2005) and by Pestalozzi et al. (2004) for the  $\text{CH}_3\text{OH}$  masers of group A, respectively. In “Scenario A” the  $\text{CH}_3\text{OH}$  masers of group A might resemble either clumps in the

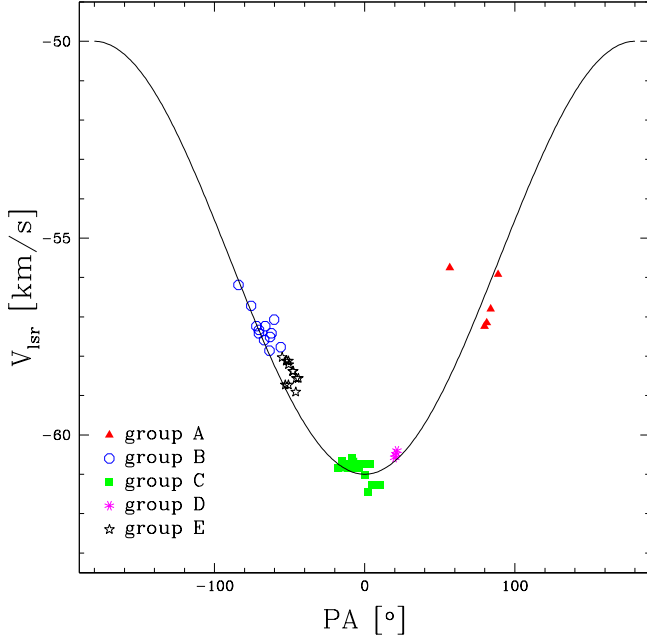


**Fig. 9.** Measured velocities of the CH<sub>3</sub>OH masers as a function of the position angle (PA) along the torus. The solid line shows the velocities of the torus reported by Klaassen et al. (2009) as function of their PA along the torus determined as described in Sect. 4.4.

cavity of the outflow or recent ejecta from the outflow, while in “Scenario B” group A trace a disk and the authors proposed a jet precession model to explain the asymmetry of the NIR emission. However, in our scenario the asymmetry of the NIR emission might reflect the innermost walls of an outflow cavity as explained in “Scenario A”, but with the masers that are tracing an infalling gas rather than the outflow cavity or a recent ejecta from the outflow.

Two questions remain: what is the radio continuum emission shown in Fig. 1? How can this scenario be consistent with the changing of the position angle of the outflow reported in Campbell (1984)? De Buizer & Minier (2005) argue that the radio continuum emission is consistent with radio emission arising from a photoevaporated disk wind and Kameya et al. (1989) suggested that the rotation of the outflow stems from a disk precession.

## 5. Conclusions

The massive star-forming region NGC7538-IRS 1 has been observed at 22-GHz in full polarization spectral mode with the VLBA and at 6.7-GHz with the EVN and MERLIN to detect linear and circular polarization emission from H<sub>2</sub>O and CH<sub>3</sub>OH masers, respectively. We detected 17 H<sub>2</sub>O masers and 49 CH<sub>3</sub>OH masers at high angular resolution. We have measured Zeeman-splitting for three CH<sub>3</sub>OH masers ranging from  $-2.7 \text{ m s}^{-1}$  to  $+2.7 \text{ m s}^{-1}$ . No significant magnetic field strength has been measured from the H<sub>2</sub>O masers. Furthermore, we have also shown that the masers of NGC7538-IRS 1 are all consistent with a torus-outflow scenario. Here the CH<sub>3</sub>OH masers are tracing the interface between the infall and the large-scale torus, and the H<sub>2</sub>O masers are related to the blue-shifted part of the outflow. The H<sub>2</sub>O masers of the southern group are thought

to be associated with another source. The magnetic field is situated on the two surfaces of the torus with a counterclockwise direction on the top surface.

**Acknowledgments.** We wish to thank an anonymous referee for making useful suggestions that have improved the paper. GS, WHTV, and RMT acknowledge support by the Deutsche Forschungsgemeinschaft (DFG) through the Emmy Noether Research grant VL 61/3-1. G.S. and WHTV thank Pamela D. Klaassen for the very useful discussion. G.S. thanks Ramiro Franco-Hernández for kindly providing the VLA continuum image.

## References

- Bartkiewicz, A., Szymczak, M., van Langevelde, H.J. et al. 2009, A&A, 502, 155
- Burns, J.O., Owen, F.N., & Rudnick, L. 1979, AJ, 84, 1683
- Campbell, B. 1984, ApJ, 282, L27
- Campbell, B. & Thompson, R. 1984, ApJ, 279, 650
- Cragg, D.M., Sobolev, A.M., & Godfrey, P.D. 2002, MNRAS, 331, 521
- Davis, C.J., Moriarty-Schieven, G., Eisloffel, J. et al. 1998, AJ, 115, 1118
- De Buizer, J.M. & Minier, V. 2005, ApJ, 628, L151
- Franco-Hernández, R. & Rodríguez, L.F. 2004, ApJ, 604, 105
- Galván-Madrid, R., Montes, G., Ramírez, E.A. et al. 2010, ApJ, 713, 423
- Gaume, R.A., Johnston, K.J., Nguyen, H.A. et al. 1991, ApJ, 376, 608
- Gaume, R.A., Goss, W.M., Dickel H.R. et al. 1995, ApJ, 438, 776
- Goldreich, P. & Keeley, D.A., 1972, ApJ, 174, 517
- Goldreich, P., Keeley, D.A., & Kwan, J.Y., 1973, ApJ, 179, 111
- Hoffman, I.M., Goss, W.M., Palmer, P. et al. 2003, ApJ, 598, 1061
- Hutawarakorn, B. & Cohen, R.J. 2003, MNRAS, 345, 175
- Kameya, O., Tatsuhiko, I.H., Hirano, N. et al. 1989, ApJ, 339, 222
- Kemball, A.J., Diamond, P.J. and Cotton, W.D. 1995, A&AS, 110, 383
- Klaassen, P.D., Wilson, C.D., Keto, E.R. et al. 2009, ApJ, 703, 1308
- Klaassen, P.D., Wilson, C.D., Keto, E.R. et al. 2011, arXiv1103.5706K
- Kraus, S., Balega, Y., Elitzur, M. et al. 2006, A&A, 455, 521
- Minier, V., Booth, R.S., and Conway, J.E. 1998, A&A, 336, L5
- Minier, V., Booth, R.S., and Conway, J.E. 2000, A&A, 362, 1093
- Minier, V., Booth, R.S., and Conway, J.E., 2002, A&A, 383, 614
- Momose, M., Tamura, M., Kameya, O. et al. 2001, ApJ, 555, 855
- Moscadelli, L., Reid, M.J., Menten, K.M. et al. 2009, ApJ, 693, 406
- Nedoluha, G.E. & Watson, W.D., 1992, ApJ, 384, 185
- Pandian, J.D., Momjian, E., Xu, Y. et al. 2011, ApJ, 730, 55
- Pestalozzi, M.R., elitzur, M., Conway, J.E. et al. 2004, ApJ, 603, L113
- Puga, E., Marín-Franch, A., Najjarro, F. et al. 2010, A&A, 517, 2
- Qiu, Keping; Zhang, Qizhou; Menten, Karl M. 2011, ApJ, 728, 6
- Sandell, G. Goss, W.M., Wright, M. et al. 2009, ApJ, 699, L31
- Scoville, N.Z., Sargent, A.I., Sanders, D.B. et al. 1986, ApJ, 303, 416
- Sun, X. H., Reich, W., Waelkens, A. et al. 2008, A&A, 477, 573
- Surcis, G., Vlemmings, W.H.T., Dodson, R. et al., 2009, A&A, 506, 757 (S09)
- Surcis, G., Vlemmings, W.H.T., Curiel, S. et al. 2011, A&A, 527, 48
- Torstenstson, K.J.E., van Langevelde, H.J., Vlemmings, W.H.T. et al. 2011, A&A, 526, 38
- Vlemmings, W.H.T., Diamond, P.J., van Langevelde, H.J. et al. 2006a, A&A, 448, 597
- Vlemmings, W.H.T. 2008, A&A, 484, 773
- Vlemmings, W.H.T., Surcis, G., Torstenstson, K.J.E. et al. 2010, MNRAS, 404, 134
- Vlemmings, W.H.T., Torres, R.M., & Dodson, R. 2011, A&A, 529, 95
- Wynn-Williams, C.G., Becklin, E.E., & Neugebauer, G. 1974, ApJ, 187, 473